

An efficient fully decoupled finite element method with second-order accuracy for the micropolar Rayleigh-Bénard convection system

Ming Cui, Akang Hou, and Xiaoyu Dong*

*Department of Mathematics, School of Mathematics, Statistics and Mechanics,
Beijing University of Technology, Beijing 100124, P.R. China*

Abstract. The micropolar Rayleigh-Bénard convection system, which consists of Navier-Stokes equations, the angular momentum equation, and the heat equation, is a strongly nonlinear, coupled, and saddle point structural multiphysics system. A second-order pressure projection finite element method, which is linear, fully decoupled, and second-order accurate in time, is proposed to simulate the system. Only a few decoupled linear elliptic problems with constant coefficients are solved at each time step, simplifying calculations significantly. The stability analysis of the method is established and the optimal error estimates are derived rigorously with the negative norm technique. Extensive numerical simulations, including 2D and 3D accuracy tests, the lid-driven cavity flow, and the passive-scalar mixing experiment, are carried out to illustrate the effectiveness of the method.

AMS subject classifications: 65M12, 65M60, 76M10

Key words: Micropolar Rayleigh-Bénard convection system, projection method, fully decoupling, unconditional stability, optimal error estimates.

1 Introduction

The micropolar fluid model, originally introduced by Eringen in 1966 [1], belongs to a class of non-Newtonian fluid theories accounting for microstructural effects and local particle rotations, which is a significant generalization of the incompressible Navier-Stokes model of classical hydrodynamics. A key feature of this model is the interaction between the rotational motion of microscopic constituents and the macroscopic velocity field. In narrow channels, the differences between the micropolar fluid model and the Navier-Stokes model become more pronounced [2, 3]. Micropolar theory effectively describes the dynamics of complex fluids with microstructural characteristics, substantially extending the range of physical phenomena captured by conventional continuum theories, such as the flow behavior of biological fluids, liquid crystals and dilute aqueous polymer solutions [4]. In recent years, many scholars have studied the dynamics of fluid layers between two

*Corresponding author. *Email addresses:* mingcui@bjut.edu.cn (M. Cui), houakang@emails.bjut.edu.cn (A. Hou), dongxy@bjut.edu.cn (X. Dong)

rigid boundaries heated from below, which is a basic problem in thermal convection. To capture thermally driven flow accurately, in this work, we focus on a mathematical model based on the Boussinesq approximation which describes the heat convection in a micropolar fluid, which is called a micropolar Rayleigh-Bénard convection system [5, 6, 7, 8].

The micropolar Rayleigh-Bénard convection system provides a more accurate description of microscale flow and angular momentum transport driven by temperature gradients, enhancing the thermal control efficiency and system design. Therefore, it has significant applications in engineering fields such as microelectronic cooling, biomedical hyperthermia, ferrofluid-based thermal management, and polymer processing [7, 9, 10, 11]. Many problems in engineering, especially those involving coupled heat transfer, often exhibit strongly nonlinear characteristics. Although certain cases can be solved analytically, most of these issues require numerical methods such as the perturbation method, the homotopy perturbation method, the variational iteration approach [12], and the finite difference method [13]. At present, few numerical techniques are available for the micropolar Rayleigh-Bénard convection system. The finite element method is employed to discretize the highly linear micropolar Rayleigh-Bénard convection system in this work. To overcome the difficulty due to the saddle point structure formed by velocity and pressure, we adopt a pressure projection technique, which was first introduced by Chorin [14] and was confirmed to be an effective approach to overcome such challenges in the late 1960s [15]. This method is based on a rather peculiar time-discretization of the equations governing viscous incompressible flows, in which the viscosity and the incompressibility of the fluid are treated within two separate steps. As shown in [16], the projection algorithm can also be interpreted as a pressure stabilization technique. In practice, this technique is compatible with various spatial discretizations, including spectral approximations [17] and finite differences [18]. Currently, the hybrid scheme of this approach with the finite element method has been widely used by researchers to address various types of problems. Guermond [19] investigated a div-grad problem, employing velocity test functions that satisfy various boundary conditions, and supplemented the formulation for a Poisson equation subject to a Neumann boundary condition. Furthermore, a fractional-step projection method for incompressible viscous flows using finite element approximations was analyzed in [20] which established finite-time error estimates and illustrated the flexibility of the method through examples involving nonstandard boundary conditions. Then a second-order pressure projection finite element scheme was proposed for the Navier-Stokes equations in [21], and the optimal error estimate was provided. A series of studies in [22, 23, 24] applied the projection method with the finite element method to two-phase FHD Shliomis models. For more information about the application of the projection method, please refer to [8, 25, 26, 27, 28, 29]. For the existence of solutions, the global regularity for the 2D micropolar Rayleigh-Bénard convection system with zero diffusivity was given in [30] and the well-posedness of the 2D micropolar Rayleigh-Bénard convection problem was established in [31]. In [32], the global regularity for the 2D micropolar Rayleigh-Bénard convection system is provided with zero velocity dissipation and critical temperature diffusion. These theoretical researches become excellent foundations for numerical schemes to solve the micropolar Rayleigh-Bénard convection system.

The rest of this paper is organized as follows. We first introduce the micropolar Rayleigh-Bénard convection system and preliminaries in Section 2, and then develop a second-order pres-

sure projection method to solve the micropolar Rayleigh-Bénard convection system and prove its unconditional stability in Section 3. In Section 4, the optimal error estimates of the numerical scheme are presented. Numerical tests are carried out in Section 5 to verify the effectiveness of the method.

2 The micropolar Rayleigh-Bénard convection system

The micropolar Rayleigh-Bénard convection system is formulated as

$$\begin{cases} \mathbf{u}_t + (\mathbf{u} \cdot \nabla) \mathbf{u} - (\chi + \mu) \Delta \mathbf{u} + \nabla p = 2\chi \nabla \times \boldsymbol{\omega} + \theta \mathbf{e}, \\ \nabla \cdot \mathbf{u} = 0, \\ \zeta \boldsymbol{\omega}_t + \zeta (\mathbf{u} \cdot \nabla) \boldsymbol{\omega} - \nu \Delta \boldsymbol{\omega} - \eta \nabla (\nabla \cdot \boldsymbol{\omega}) + 4\chi \boldsymbol{\omega} = 2\chi \nabla \times \mathbf{u}, \\ \theta_t + (\mathbf{u} \cdot \nabla) \theta - \kappa \Delta \theta = \mathbf{u} \cdot \mathbf{e}. \end{cases} \quad (2.1)$$

The unknown physical variables are the velocity field \mathbf{u} , pressure p , the angular velocity field $\boldsymbol{\omega}$, and temperature θ . The parameters $\chi, \mu, \nu, \eta, \zeta$ and κ are the Newtonian kinematic viscosity, the micro-rotation viscosity, the angular viscosity, the inertia density, and the thermal diffusivity, respectively. \mathbf{e} is the unit vector where $\mathbf{e} = (0, 1)$ in 2D and $\mathbf{e} = (0, 0, 1)$ in 3D, $\theta \mathbf{e}$ describes the action of the buoyancy force on fluid motion and $\mathbf{u} \cdot \mathbf{e}$ denotes the Rayleigh-Bénard convection in a heated inviscid fluid.

For convenience, the symbols and function spaces used in the following are defined. The inner product of L^2 is defined as $(\mathbf{a}, \mathbf{b}) = \int_{\Omega} \mathbf{a} \cdot \mathbf{b} \, dx$, and the corresponding L^2 -norm, H^1 -norm and H^2 -norm are denoted by $\|\mathbf{a}\|_0$, $\|\mathbf{a}\|_1$ and $\|\mathbf{a}\|_2$, respectively. The Sobolev spaces are introduced by [33, 34, 35]

$$\begin{aligned} \mathbf{X} &:= H_0^1(\Omega)^d, \quad d=2,3, \\ \mathbf{V} &:= \{\mathbf{v} \in \mathbf{X} : \nabla \cdot \mathbf{v} = 0, \mathbf{v}|_{\partial\Omega} = \mathbf{0}\}, \\ \mathbf{V}_1 &:= \left\{ \mathbf{v} \in L^2(\Omega)^d : \nabla \cdot \mathbf{v} = 0, \mathbf{v} \cdot \mathbf{n}|_{\partial\Omega} = 0 \right\}, \quad d=2,3 \\ M &:= L_0^2(\Omega) = \left\{ \varphi \in L^2(\Omega) : \int_{\Omega} \varphi \, dx = 0 \right\}. \end{aligned}$$

Lemma 2.1 (div-grad relation inequality [25, 26]). *Let Ω be a bounded Lipschitz domain such that for all $\mathbf{v} \in \mathbf{X}$,*

$$\|\nabla \cdot \mathbf{v}\|_0 \leq \|\nabla \mathbf{v}\|_0.$$

The Stokes operator is defined as $\mathcal{A} : D(\mathcal{A}) \rightarrow \mathbf{V}_1$, such that $\mathcal{A} = -P\Delta$, where $D(\mathcal{A}) = H^2(\Omega)^d \cap \mathbf{V}$ and the L^2 -projection $P : L^2(\Omega)^d \rightarrow \mathbf{V}_1$. The following inequalities are presented in [27, 36, 37], which will be used frequently:

$$\begin{aligned} \|\mathbf{v}\|_{L^r} &\leq c(r) \|\nabla \mathbf{v}\|_0, \quad r \in [1, 6], \quad \forall \mathbf{v} \in \mathbf{X}, \\ \|\mathbf{v}\|_{L^\infty} + \|\nabla \mathbf{v}\|_{L^3} &\leq C \|\mathbf{v}\|_1^{\frac{1}{2}} \|\mathcal{A} \mathbf{v}\|_0^{\frac{1}{2}}, \quad \|\mathbf{v}\|_2 \leq C \|\mathcal{A} \mathbf{v}\|_0, \quad \forall \mathbf{v} \in D(\mathcal{A}). \end{aligned}$$

Let the bilinear forms be

$$a(\mathbf{u}, \mathbf{v}) = (\nabla \mathbf{u}, \nabla \mathbf{v}), \quad d(\mathbf{v}, p) = (\nabla \cdot \mathbf{v}, p), \quad \mathbf{B}(\mathbf{u}, \mathbf{v}) = (\mathbf{u} \cdot \nabla) \mathbf{v} + \frac{1}{2}(\nabla \cdot \mathbf{u}) \mathbf{v}, \quad \forall \mathbf{u}, \mathbf{v} \in \mathbf{X}, p \in M,$$

where $\mathbf{B}(\mathbf{u}, \mathbf{v})$ is the skew-symmetric form of the nonlinear convective terms. Assuming that the velocity field \mathbf{u} is divergence-free, the nonlinear terms reduce to $\mathbf{B}(\mathbf{u}, \mathbf{v}) = (\mathbf{u} \cdot \nabla) \mathbf{v}$. We define a trilinear form as

$$b(\mathbf{u}, \mathbf{v}, \mathbf{w}) = (\mathbf{B}(\mathbf{u}, \mathbf{v}), \mathbf{w}) = ((\mathbf{u} \cdot \nabla) \mathbf{v}, \mathbf{w}) + \frac{1}{2}((\nabla \cdot \mathbf{u}) \mathbf{v}, \mathbf{w}) = \frac{1}{2}((\mathbf{u} \cdot \nabla) \mathbf{v}, \mathbf{w}) - \frac{1}{2}((\mathbf{u} \cdot \nabla) \mathbf{w}, \mathbf{v}).$$

To ensure the well-posedness and stability of the mixed formulation, the velocity–pressure pair (\mathbf{X}, M) must satisfy the classical *inf-sup* condition [38]. Specifically, it requires that there exists a positive constant β_0 , independent of the mesh size, such that

$$\exists \beta_0 > 0, \forall q \in M, \quad \beta_0 \|q\|_0 \leq \sup_{\mathbf{v} \in \mathbf{X}, \mathbf{v} \neq \mathbf{0}} \frac{d(\mathbf{v}, q)}{\|\nabla \mathbf{v}\|_0}.$$

To derive the theoretical stability and error estimates of a numerical scheme, it is common to assume certain regularity for the exact solution and the initial values. These assumptions are reasonable since the initial values used in the numerical scheme are equal to those of the exact solution.

Assumption (A.1) ([27, 29, 37, 39]). The initial values $\mathbf{u}_0, \boldsymbol{\omega}_0$ and θ_0 satisfy

$$\|\mathcal{A}\mathbf{u}_0\|_0 + \|\boldsymbol{\omega}_0\|_0 + \|\theta_0\|_2 \leq C.$$

Assumption (A.2) ([27, 29, 37, 39]). Assuming that $(\mathbf{u}, p, \boldsymbol{\omega}, \theta)$ is a unique local strong solution of the micropolar Rayleigh–Bénard convection system (2.1) on $[0, T]$, there holds that

$$\begin{aligned} & \sup_{0 \leq t \leq T} (\|\mathcal{A}\mathbf{u}_t\|_0 + \|\boldsymbol{\omega}_t\|_0 + \|\theta_t\|_2 + \|\mathbf{u}_t\|_0 + \|\boldsymbol{\omega}_t\|_0 + \|p_t\|_1 + \|\mathcal{A}\mathbf{u}\|_0 + \|\boldsymbol{\omega}\|_0 + \|\nabla \mathbf{u}\|_{L^\infty} \\ & + \|\nabla \boldsymbol{\omega}\|_{L^\infty} + \|\nabla \theta\|_{L^\infty}) + \int_0^T (\|\mathbf{u}_t\|_1^2 + \|\boldsymbol{\omega}_t\|_1^2 + \|\theta_t\|_1^2 + \|\mathbf{u}_{tt}\|_0^2 + \|\boldsymbol{\omega}_{tt}\|_0^2 + \|\theta_{tt}\|_0^2 \\ & + \|\mathbf{u}_{ttt}\|_0^2 + \|\boldsymbol{\omega}_{ttt}\|_0^2 + \|\theta_{ttt}\|_0^2 + \|p_t\|_1^2) dt \leq C. \end{aligned}$$

Lemma 2.2 ([37]). Let a_n, b_n, c_n and γ_n , for integer $n \geq 0$, be the nonnegative numbers such that

$$a_m + \delta_t \sum_{n=0}^m b_n \leq \delta_t \sum_{n=0}^m \gamma_n a_n + \delta_t \sum_{n=0}^m c_n + B, \quad \forall m \geq 0.$$

Suppose that $\delta_t \gamma_n < 1$, for all n , and set $\sigma_n = (1 - \delta_t \gamma_n)^{-1}$. Then

$$a_m + \delta_t \sum_{n=0}^m b_n \leq \exp(\delta_t \sum_{n=0}^m \gamma_n \sigma_n) (\delta_t \sum_{n=0}^m c_n + B), \quad \forall m \geq 0.$$

3 Numerical scheme and Stability analysis

A pressure-projection finite element scheme, which is unconditionally stable, fully decoupled, linear, and second-order accurate in time, is constructed for (2.1). In this section, the numerical scheme and stability in fully discrete form are presented.

3.1 Second-order pressure projection scheme

Let T_h be a family of regular and quasi-uniform triangulation partition of Ω , consisting of tetrahedral elements K , where $h = \max_{K \in T_h} h_K$ and h_K is the diameter of the element K [33, 34, 35]. The scalar and vector finite element space are

$$\begin{aligned} X_h &:= \{v_h \in C^0(\Omega)^d : v_h|_K \in P_k(K)^d, \forall K \in T_h\} \cap H_0^1(\Omega)^d, \\ V_h &:= \{v_h \in C^0(\Omega)^d : v_h|_K \in P_k(K)^d, \forall K \in T_h\} \cap V, \\ M_h &:= \{q_h \in C^0(\Omega) : q_h|_K \in P_l(K), \forall K \in T_h\} \cap L_0^2(\Omega), \\ W_h &:= \{\Lambda_h \in C^0(\Omega)^d : \Lambda_h|_K \in P_r(K)^d, \forall K \in T_h\} \cap H_0^1(\Omega)^d, \\ \mathcal{T}_h &:= \{\psi_h \in C^0(\Omega) : \psi_h|_K \in P_s(K), \forall K \in T_h\} \cap H_0^1(\Omega). \end{aligned}$$

where $P_k(K), P_l(K), P_r(K)$ and $P_s(K)$ represent spaces of polynomials with degree bounded uniformly with respect to $K \in T_h$ and $d=2,3$. Let $0 = t^0 < t^1 < \dots < t^{N+1} = T$ be a uniform partition of the time interval $[0, T]$ with $t^n = n\delta_t$.

The core idea of the second-order pressure projection method is to split the pressure term from the momentum equation. Firstly, a prediction for the velocity field is computed. Then pressure and velocity corrections are performed to enforce the divergence-free constraint. Finally, the angular velocity and temperature fields are updated independently. Details are shown in the following.

Starting with the initial solution $(u_h^0, \omega_h^0, \theta_h^0, p_h^0)$, the discrete initial conditions are defined by

$$\begin{aligned} (\tilde{u}_h^0, v_h) &= (u_h^0, v_h) = (u_0, v_h), \quad (\omega_h^0, \Lambda_h) = (\omega_0, \Lambda_h), \quad (\theta_h^0, \psi_h) = (\theta_0, \psi_h), \\ \nabla p_h^0 &= (\chi + \mu) \Delta u_h^0 - u_h^0 \cdot \nabla u_h^0 + 2\chi \nabla \times \omega_h^0 + \theta_h^0 e. \end{aligned} \quad (3.1)$$

For $(u_h^1, \omega_h^1, \theta_h^1)$, a first-order pressure projection scheme [22] can be derived based on (3.1).

Step 1. Find $\tilde{u}_h^{n+1} \in X_h$ such that for all $v_h \in X_h$,

$$\begin{aligned} \left(\frac{3\tilde{u}_h^{n+1} - 4u_h^n + u_h^{n-1}}{2\delta_t}, v_h \right) &+ (\chi + \mu) (\nabla \tilde{u}_h^{n+1}, \nabla v_h) + ((\tilde{u}_h^n \cdot \nabla) \tilde{u}_h^{n+1}, v_h) \\ &+ (\nabla p_h^n, v_h) = 2\chi (\nabla \times \bar{\omega}_h^n, v_h) + (\bar{\theta}_h^n e, v_h). \end{aligned} \quad (3.2)$$

where $\bar{\omega}_h^n = 2\omega_h^n - \omega_h^{n-1}$ and $\bar{\theta}_h^n = 2\theta_h^n - \theta_h^{n-1}$.

Step 2. Find $p_h^{n+1} \in M_h$ such that for all $q_h \in M_h$,

$$(\nabla p_h^{n+1}, \nabla q_h) = -\frac{3}{2\delta_t} (\nabla \cdot \tilde{u}_h^{n+1}, q_h) + (\nabla p_h^n, \nabla q_h). \quad (3.3)$$

Step 3. Update $\mathbf{u}_h^{n+1} \in \mathbf{X}_h \oplus \nabla M_h$ by

$$\mathbf{u}_h^{n+1} = \tilde{\mathbf{u}}_h^{n+1} - \frac{2\delta_t}{3} \nabla p_h^{n+1} + \frac{2\delta_t}{3} \nabla p_h^n. \quad (3.4)$$

Step 4. Find $\boldsymbol{\omega}_h^{n+1} \in \mathbf{W}_h$ such that for all $\Lambda_h \in \mathbf{W}_h$,

$$\begin{aligned} \zeta \left(\frac{3\boldsymbol{\omega}_h^{n+1} - 4\boldsymbol{\omega}_h^n + \boldsymbol{\omega}_h^{n-1}}{2\delta_t}, \Lambda_h \right) + v(\nabla \boldsymbol{\omega}_h^{n+1}, \nabla \Lambda_h) + \zeta((\bar{\mathbf{u}}_h^n \cdot \nabla) \boldsymbol{\omega}_h^{n+1}, \Lambda_h) \\ + \eta(\nabla \cdot \boldsymbol{\omega}_h^{n+1}, \nabla \cdot \Lambda_h) + 4\chi(\boldsymbol{\omega}_h^{n+1}, \Lambda_h) = 2\chi(\nabla \times \bar{\mathbf{u}}_h^n, \Lambda_h). \end{aligned} \quad (3.5)$$

where $\bar{\mathbf{u}}_h^n = 2\mathbf{u}_h^n - \mathbf{u}_h^{n-1}$.

Step 5. Find $\theta_h^{n+1} \in \mathcal{T}_h$ such that for all $\psi_h \in \mathcal{T}_h$,

$$\left(\frac{3\theta_h^{n+1} - 4\theta_h^n + \theta_h^{n-1}}{2\delta_t}, \psi_h \right) + \kappa(\nabla \theta_h^{n+1}, \nabla \psi_h) + ((\bar{\mathbf{u}}_h^n \cdot \nabla) \theta_h^{n+1}, \psi_h) = (\bar{\mathbf{u}}_h^n \cdot \mathbf{e}, \psi_h). \quad (3.6)$$

The advantage of the numerical scheme (3.1)-(3.6) lies in the linearity and fully decoupling, and \mathbf{u} , p , $\boldsymbol{\omega}$ and θ can be solved linearly and independently at each time step, providing a feasible numerical approach to solve equations (2.1) efficiently.

3.2 Stability analysis

In this subsection, the stability analysis of the second-order pressure projection scheme (3.1)–(3.6) is presented.

Theorem 3.1. *Suppose that Assumptions (A.1)-(A.2) are satisfied, the scheme is unconditionally stable, for all $\delta_t > 0$, there exists a prior bound such that*

$$\begin{aligned} & \|\mathbf{u}_h^{N+1}\|_0^2 + \|2\mathbf{u}_h^{N+1} - \mathbf{u}_h^N\|_0^2 + \zeta\|\boldsymbol{\omega}_h^{N+1}\|_0^2 + \zeta\|2\boldsymbol{\omega}_h^{N+1} - \boldsymbol{\omega}_h^N\|_0^2 + \|\theta_h^{N+1}\|_0^2 + \|2\theta_h^{N+1} - \theta_h^N\|_0^2 \\ & + \delta_t \sum_{n=1}^N \left(\|\mathbf{u}_h^{n+1} - 2\mathbf{u}_h^n + \mathbf{u}_h^{n-1}\|_0^2 + (\chi + \mu) \|\nabla \tilde{\mathbf{u}}_h^{n+1}\|_0^2 + \zeta\|\boldsymbol{\omega}_h^{n+1} - 2\boldsymbol{\omega}_h^n + \boldsymbol{\omega}_h^{n-1}\|_0^2 + v\|\nabla \boldsymbol{\omega}_h^{n+1}\|_0^2 \right. \\ & \left. + 8\eta\|\nabla \cdot \boldsymbol{\omega}_h^{n+1}\|_0^2 + 16\chi\|\boldsymbol{\omega}_h^{n+1}\|_0^2 + \|\theta_h^{n+1} - 2\theta_h^n + \theta_h^{n-1}\|_0^2 + \kappa\|\nabla \theta_h^{n+1}\|_0^2 \right) + \frac{\delta_t^2}{3} \|\nabla p^{N+1}\|_0^2 \\ & \leq \left(\|\mathbf{u}_h^0\|_0^2 + \|2\mathbf{u}_h^1 - \mathbf{u}_h^0\|_0^2 + \zeta\|\boldsymbol{\omega}_h^0\|_0^2 + \zeta\|2\boldsymbol{\omega}_h^1 - \boldsymbol{\omega}_h^0\|_0^2 + \|\theta_h^0\|_0^2 + \|2\theta_h^1 - \theta_h^0\|_0^2 \right) \\ & + C\delta_t(\|\bar{\mathbf{u}}_h^n\|_0^2 + \|\bar{\boldsymbol{\omega}}_h^n\|_0^2 + \|\bar{\theta}_h^n\|_0^2) + \frac{4\delta_t^2}{3} \|\nabla p_h^0\|_0^2, \end{aligned}$$

where C is a positive constant independent of h and δ_t .

Proof. Setting $v_h = 4\delta_t \tilde{u}_h^{n+1}$ in (3.2), $\Lambda_h = 4\delta_t \omega_h^{n+1}$ in (3.5), and $\psi_h = 4\delta_t \theta_h^{n+1}$ in (3.6), respectively, there are

$$\begin{aligned} 2(3\tilde{u}_h^{n+1} - 4u_h^n + u_h^{n-1}, \tilde{u}_h^{n+1}) + 4(\chi + \mu)\delta_t \|\nabla \tilde{u}_h^{n+1}\|_0^2 + 4\delta_t (\nabla p_h^n, \tilde{u}_h^{n+1}) \\ = 8\chi\delta_t (\nabla \times \bar{\omega}_h^n, \tilde{u}_h^{n+1}) + 4\delta_t (\bar{\theta}_h^n e, \tilde{u}_h^{n+1}), \end{aligned} \quad (3.7)$$

$$\begin{aligned} 2\zeta(3\omega_h^{n+1} - 4\omega_h^n + \omega_h^{n-1}, \omega_h^{n+1}) + 4v\delta_t \|\nabla \omega_h^{n+1}\|_0^2 + 4\eta\delta_t \|\nabla \cdot \omega_h^{n+1}\|_0^2 + 16\chi\delta_t \|\omega_h^{n+1}\|_0^2 \\ = 8\chi\delta_t (\nabla \times \bar{u}_h^n, \omega_h^{n+1}), \end{aligned} \quad (3.8)$$

$$2(3\theta_h^{n+1} - 4\theta_h^n + \theta_h^{n-1}, \theta_h^{n+1}) + 4\kappa\delta_t \|\nabla \theta_h^{n+1}\|_0^2 = 4\delta_t (\bar{u}_h^n \cdot e, \theta_h^{n+1}). \quad (3.9)$$

From the weak divergence-free condition of u_h^{n+1} , along with the identity

$$2(3a - 4b + c, a) = |a|^2 - |b|^2 + |2a - b|^2 - |2b - c|^2 + |a + 2b - c|^2$$

and (3.4), we obtain

$$\begin{aligned} 2(3\tilde{u}_h^{n+1} - 4u_h^n + u_h^{n-1}, \tilde{u}_h^{n+1}) = \|u_h^{n+1}\|_0^2 - \|u_h^n\|_0^2 + \|2u_h^{n+1} - u_h^n\|_0^2 - \|2u_h^n - u_h^{n-1}\|_0^2 \\ + \|u_h^{n+1} - 2u_h^n + u_h^{n-1}\|_0^2 + 6\|\tilde{u}_h^{n+1} - u_h^{n+1}\|_0^2. \end{aligned} \quad (3.10)$$

We rewrite (3.4) as

$$u_h^{n+1} + \frac{2}{3}\delta_t \nabla p_h^{n+1} = \tilde{u}_h^{n+1} + \frac{2}{3}\delta_t \nabla p_h^n, \quad (3.11)$$

by taking the L^2 inner product of (3.11) with itself and applying relation (3.3), we get

$$(\nabla p_h^n, \tilde{u}_h^{n+1}) = \frac{3}{4\delta_t} \|u_h^{n+1}\|_0^2 - \frac{3}{4\delta_t} \|\tilde{u}_h^{n+1}\|_0^2 + \frac{\delta_t}{3} \|\nabla p_h^{n+1}\|_0^2 - \frac{\delta_t}{3} \|\nabla p_h^n\|_0^2, \quad (3.12)$$

From (3.7)-(3.12), one obtains

$$\begin{aligned} \|u_h^{n+1}\|_0^2 - \|u_h^n\|_0^2 + \|2u_h^{n+1} - u_h^n\|_0^2 - \|2u_h^n - u_h^{n-1}\|_0^2 + \|u_h^{n+1} - 2u_h^n + u_h^{n-1}\|_0^2 + 6\|\tilde{u}_h^{n+1} - u_h^{n+1}\|_0^2 \\ + 4(\chi + \mu)\delta_t \|\nabla \tilde{u}_h^{n+1}\|_0^2 + \zeta \|\omega_h^{n+1}\|_0^2 - \zeta \|\omega_h^n\|_0^2 + \zeta \|2\omega_h^{n+1} - \omega_h^n\|_0^2 - \zeta \|2\omega_h^n - \omega_h^{n-1}\|_0^2 \\ + \zeta \|\omega_h^{n+1} - 2\omega_h^n + \omega_h^{n-1}\|_0^2 + 4v\delta_t \|\nabla \omega_h^{n+1}\|_0^2 + 4\eta\delta_t \|\nabla \cdot \omega_h^{n+1}\|_0^2 + 16\chi\delta_t \|\omega_h^{n+1}\|_0^2 \\ + \|\theta_h^{n+1}\|_0^2 - \|\theta_h^n\|_0^2 + \|2\theta_h^{n+1} - \theta_h^n\|_0^2 - \|2\theta_h^n - \theta_h^{n-1}\|_0^2 + \|\theta_h^{n+1} - 2\theta_h^n + \theta_h^{n-1}\|_0^2 \\ + 4\kappa\delta_t \|\nabla \theta_h^{n+1}\|_0^2 + \frac{4\delta_t^2}{3} (\|\nabla p_h^{n+1}\|_0^2 - \|\nabla p_h^n\|_0^2) + 3\|\tilde{u}_h^{n+1} - u_h^{n+1}\|_0^2 \\ = 8\chi\delta_t (\nabla \times \bar{\omega}_h^n, \tilde{u}_h^{n+1}) + 4\delta_t (\bar{\theta}_h^n e, \tilde{u}_h^{n+1}) + 8\chi\delta_t (\nabla \times \bar{u}_h^n, \omega_h^{n+1}) + 4\delta_t (\bar{u}_h^n \cdot e, \theta_h^{n+1}). \end{aligned} \quad (3.13)$$

Invoking Hölder's inequality and Young's inequality,

$$\begin{aligned} |4\chi\delta_t(\nabla \times \bar{\omega}_h^n, \tilde{\mathbf{u}}_h^{n+1})| &= |4\chi\delta_t(\bar{\omega}_h^n, \nabla \times \tilde{\mathbf{u}}_h^{n+1})| \\ &\leq C\delta_t \|\bar{\omega}_h^n\|_0 \|\nabla \tilde{\mathbf{u}}_h^{n+1}\|_0 \leq \frac{3(\chi+\mu)}{2} \delta_t \|\nabla \tilde{\mathbf{u}}_h^{n+1}\|_0^2 + C\delta_t \|\bar{\omega}_h^n\|_0^2, \end{aligned} \quad (3.14)$$

$$|4\delta_t(e\bar{\theta}_h^n, \tilde{\mathbf{u}}_h^{n+1})| \leq C\delta_t \|\bar{\theta}_h^n\|_0 \|\nabla \tilde{\mathbf{u}}_h^{n+1}\|_0 \leq \frac{3(\chi+\mu)}{2} \delta_t \|\nabla \tilde{\mathbf{u}}_h^{n+1}\|_0^2 + C\delta_t \|\bar{\theta}_h^n\|_0^2, \quad (3.15)$$

$$|8\chi\delta_t(\nabla \times \bar{\mathbf{u}}_h^n, \omega_h^{n+1})| \leq C\delta_t \|\bar{\mathbf{u}}_h^n\|_0 \|\nabla \omega_h^{n+1}\|_0 \leq 3v\delta_t \|\nabla \omega_h^{n+1}\|_0^2 + C\delta_t \|\bar{\mathbf{u}}_h^n\|_0^2, \quad (3.16)$$

$$|4\delta_t(\bar{\mathbf{u}}_h^n \cdot \mathbf{e}, \theta_h^{n+1})| \leq C\delta_t \|\bar{\mathbf{u}}_h^n\|_0 \|\nabla \theta_h^{n+1}\|_0 \leq 3\kappa\delta_t \|\nabla \theta_h^{n+1}\|_0^2 + C\delta_t \|\bar{\mathbf{u}}_h^n\|_0^2. \quad (3.17)$$

Combining (3.13)-(3.17) and summing up from $n=0$ to N , we derive

$$\begin{aligned} &\|\mathbf{u}_h^{N+1}\|_0^2 + \|2\mathbf{u}_h^{N+1} - \mathbf{u}_h^N\|_0^2 + \zeta \|\omega_h^{N+1}\|_0^2 + \zeta \|2\omega_h^{N+1} - \omega_h^N\|_0^2 + \|\theta_h^{N+1}\|_0^2 + \|2\theta_h^{N+1} - \theta_h^N\|_0^2 \\ &+ \sum_{n=0}^{n+1} (9\|\tilde{\mathbf{u}}_h^{n+1} - \mathbf{u}_h^{n+1}\|_0^2 + \|\mathbf{u}_h^{n+1} - 2\mathbf{u}_h^n + \mathbf{u}_h^{n-1}\|_0^2 + \|\theta_h^{n+1} - 2\theta_h^n + \theta_h^{n-1}\|_0^2 \\ &+ \zeta \|\omega_h^{n+1} - 2\omega_h^n + \omega_h^{n-1}\|_0^2 + (\chi+\mu)\delta_t \|\nabla \tilde{\mathbf{u}}_h^{n+1}\|_0^2 + v\delta_t \|\nabla \omega_h^{n+1}\|_0^2 + 4\eta\delta_t \|\nabla \cdot \omega_h^{n+1}\|_0^2 \\ &+ 16\chi\delta_t \|\omega_h^{n+1}\|_0^2 + \kappa\delta_t \|\nabla \theta_h^{n+1}\|_0^2) + \frac{4\delta_t^2}{3} \|\nabla p_h^{N+1}\|_0^2 \\ &\leq \|\mathbf{u}_h^0\|_0^2 + \|2\mathbf{u}_h^1 - \mathbf{u}_h^0\|_0^2 + \zeta \|\omega_h^0\|_0^2 + \zeta \|2\omega_h^1 - \omega_h^0\|_0^2 + \|\theta_h^0\|_0^2 + \|2\theta_h^1 - \theta_h^0\|_0^2 + \frac{4\delta_t^2}{3} \|\nabla p_h^0\|_0^2 \\ &+ \sum_{n=0}^{n+1} (C\delta_t \|\bar{\mathbf{u}}_h^n\|_0^2 + C\delta_t \|\bar{\omega}_h^n\|_0^2 + C\delta_t \|\bar{\theta}_h^n\|_0^2). \end{aligned}$$

In light of Grönwall's lemma, the proof is completed. \square

4 Error estimates

In this section, the convergence analysis of the fully discrete scheme (3.1)-(3.6) is presented. We first derive suboptimal error estimates for the velocity, magnetic field, and angular velocity. Then, by introducing the inverse Stokes operator together with the dual-norm technique, we overcome the convergence-order reduction caused by the pressure term and subsequently obtain optimal error estimates.

In the error analysis, the exact solutions at time t^{n+1} are denoted as $\mathbf{u}(t^{n+1})$, $\omega(t^{n+1})$, $p(t^{n+1})$,

and $\theta(t^{n+1})$. From (2.1), we obtain

$$\begin{aligned} \frac{3\mathbf{u}(t^{n+1}) - 4\mathbf{u}(t^n) + \mathbf{u}(t^{n-1}))}{2\delta_t} - (\chi + \mu)\Delta\mathbf{u}(t^{n+1}) + (\mathbf{u}(t^{n+1}) \cdot \nabla)\mathbf{u}(t^{n+1}) + \nabla p(t^{n+1}) \\ = 2\chi(\nabla \times \boldsymbol{\omega}(t^{n+1})) + \theta(t^{n+1})\mathbf{e} + R_u^{n+1}, \end{aligned} \quad (4.1)$$

$$\nabla \cdot \mathbf{u}(t^{n+1}) = 0, \quad (4.2)$$

$$\begin{aligned} \zeta \frac{3\boldsymbol{\omega}(t^{n+1}) - 4\boldsymbol{\omega}(t^n) + \boldsymbol{\omega}(t^{n-1}))}{2\delta_t} - v\Delta\boldsymbol{\omega}(t^{n+1}) + \zeta(\mathbf{u}(t^{n+1}) \cdot \nabla)\boldsymbol{\omega}(t^{n+1}) \\ - \eta\nabla(\nabla \cdot \boldsymbol{\omega}(t^{n+1})) + 4\chi\boldsymbol{\omega}(t^{n+1}) = 2\chi\nabla \times \mathbf{u}(t^{n+1}) + R_\omega^{n+1}, \end{aligned} \quad (4.3)$$

$$\frac{3\theta(t^{n+1}) - 4\theta(t^n) + \theta(t^{n-1}))}{2\delta_t} - \kappa\Delta\theta(t^{n+1}) + (\mathbf{u}(t^{n+1}) \cdot \nabla)\theta(t^{n+1}) = \mathbf{u}(t^{n+1}) \cdot \mathbf{e} + R_\theta^{n+1}, \quad (4.4)$$

where

$$\begin{aligned} R_u^{n+1} &= \frac{3\mathbf{u}(t^{n+1}) - 4\mathbf{u}(t^n) + \mathbf{u}(t^{n-1}))}{2\delta_t} - \mathbf{u}_t(t^{n+1}), & R_\omega^{n+1} &= \frac{3\boldsymbol{\omega}(t^{n+1}) - 4\boldsymbol{\omega}(t^n) + \boldsymbol{\omega}(t^{n-1}))}{2\delta_t} - \boldsymbol{\omega}_t(t^{n+1}), \\ R_\theta^{n+1} &= \frac{3\theta(t^{n+1}) - 4\theta(t^n) + \theta(t^{n-1}))}{2\delta_t} - \theta_t(t^{n+1}). \end{aligned}$$

To meet the requirements of the fully discrete error analysis, the Stokes projection is defined by [37]

$$(R_h(\mathbf{v}, q), Q_h(\mathbf{v}, q)) : (\mathbf{X}, M) \longrightarrow (\mathbf{X}_h, M_h)$$

satisfying

$$\begin{aligned} v(\nabla(R_h(\mathbf{v}, q) - \mathbf{v}), \nabla \mathbf{v}_h) - (Q_h(\mathbf{v}, q) - q, \nabla \cdot \mathbf{v}_h) &= 0, \quad \forall \mathbf{v}_h \in \mathbf{X}_h, \\ (\nabla \cdot (R_h(\mathbf{u}, p) - \mathbf{u}), q_h) &= 0, \quad \forall q_h \in M_h. \end{aligned}$$

Assume that $\mathbf{v} \in H_0^2(\Omega)^d \cap H^{r+1}(\Omega)^d$ and $q \in L_0^2(\Omega) \cap H^r(\Omega)$ ($d = 2, 3$), the Stokes projection satisfies the estimate

$$\begin{aligned} \|R_h(\mathbf{v}, q) - \mathbf{v}\|_0 + h(\|\nabla(R_h(\mathbf{v}, q) - \mathbf{v})\|_0 + \|Q_h(\mathbf{v}, q) - q\|_0) &\leq Ch^{r+1}(\|\mathbf{v}\|_{r+1} + \|q\|_r), \\ \|R_h(\mathbf{v}, q)\|_{L^\infty} + \|\nabla R_h(\mathbf{v}, p)\|_{L^3} &\leq C(\|\mathbf{v}\|_2 + \|q\|_1), \\ \|\partial_t \nabla(R_h(\mathbf{v}, q) - \mathbf{v})\|_0 + h\|\partial_t \nabla(Q_h(\mathbf{v}, q) - q)\|_0 &\leq Ch^{r+1}(\|\partial_t \nabla \mathbf{v}\|_{r+1} + \|\partial_t \nabla q\|_r). \end{aligned}$$

Similarly, the H^1 -orthogonal projection $R_{0h} : \mathbf{X} \rightarrow \mathbf{X}_h$ is defined by

$$(\nabla R_{0h}(\mathbf{v}) - \nabla \mathbf{v}, \nabla \mathbf{w}_h) = 0, \quad \forall \mathbf{w}_h \in \mathbf{X}_h,$$

for any $\mathbf{v} \in \mathbf{X} \cap H^{r+1}(\Omega)^d$ ($d = 1, 2, 3$), the projection satisfies the estimate

$$\begin{aligned} \|R_{0h}(\mathbf{v}) - \mathbf{v}\|_0 + h\|\nabla(R_{0h}(\mathbf{v}) - \mathbf{v})\|_0 &\leq Ch^{r+1}\|\mathbf{v}\|_{r+1}, \\ \|R_{0h}(\mathbf{v})\|_{L^\infty} &\leq C\|\mathbf{v}\|_2, \quad \|\nabla R_{0h}(\mathbf{v})\|_{L^\infty} \leq C\|\mathbf{v}\|_{W^{1,\infty}}, \end{aligned}$$

for simplicity, note the residuals as that

$$\begin{aligned} R_{\omega h}^{n+1} &= R_{\omega h}(\omega(t^{n+1})), & R_{uh}^{n+1} &= R_{uh}(u(t^{n+1}), p(t^{n+1})), \\ Q_h^{n+1} &= Q_h(u(t^{n+1}), p(t^{n+1})), & R_{\theta h}^{n+1} &= R_{\theta h}(\theta(t^{n+1})), \quad n=1,2,\dots,N+1. \end{aligned}$$

Accordingly, it follows that

$$\begin{aligned} \frac{3R_{uh}^{n+1} - 4R_{uh}^n + R_{uh}^{n-1}}{2\delta_t} - (\chi + \mu)\Delta R_{uh}^{n+1} + (R_{uh}^{n+1} \cdot \nabla)R_{uh}^{n+1} + \nabla Q_h^{n+1} \\ = 2\chi \nabla \times R_{\omega h}^{n+1} + e_3 R_{\theta h}^{n+1} + R_{ul}^{n+1}, \end{aligned} \quad (4.5)$$

$$\nabla \cdot R_{uh}^{n+1} = 0, \quad (4.6)$$

$$\begin{aligned} \zeta \frac{3R_{\omega h}^{n+1} - 4R_{\omega h}^n + R_{\omega h}^{n-1}}{2\delta_t} - \nu \Delta R_{\omega h}^{n+1} + \zeta (R_{uh}^{n+1} \cdot \nabla)R_{\omega h}^{n+1} - \eta \nabla (\nabla \cdot R_{\omega h}^{n+1}) + 4\chi R_{\omega h}^{n+1} \\ = 2\chi \nabla \times R_{uh}^{n+1} + R_{\omega l}^{n+1}, \end{aligned} \quad (4.7)$$

$$\frac{3R_{\theta h}^{n+1} - 4R_{\theta h}^n + R_{\theta h}^{n-1}}{2\delta_t} - \kappa \Delta R_{\theta h}^{n+1} + (R_{uh}^{n+1} \cdot \nabla)R_{\theta h}^{n+1} = R_{uh}^{n+1} \cdot e + R_{\theta l}^{n+1}, \quad (4.8)$$

where

$$\begin{aligned} R_{ul}^{n+1} &= \frac{3R_{uh}^{n+1} - 4R_{uh}^n + R_{uh}^{n-1}}{2\delta_t} - u_t(t^{n+1}), & R_{\omega l}^{n+1} &= \frac{3R_{\omega h}^{n+1} - 4R_{\omega h}^n + R_{\omega h}^{n-1}}{2\delta_t} - \omega_t(t^{n+1}), \\ R_{\theta l}^{n+1} &= \frac{3R_{\theta h}^{n+1} - 4R_{\theta h}^n + R_{\theta h}^{n-1}}{2\delta_t} - \theta_t(t^{n+1}). \end{aligned}$$

To simplify the analysis, the relevant errors and residuals are defined by

$$\begin{aligned} \epsilon_u^{n+1} &= R_{uh}^{n+1} - u_h^{n+1}, & \tilde{\epsilon}_u^{n+1} &= R_{uh}^{n+1} - \tilde{u}_h^{n+1}, & \epsilon_\omega^{n+1} &= R_{\omega h}^{n+1} - \omega_h^{n+1}, \\ \epsilon_\theta^{n+1} &= R_{\theta h}^{n+1} - \theta_h^{n+1}, & \epsilon_p^{n+1} &= Q_h^{n+1} - p_h^{n+1}, \\ \bar{\epsilon}_u^n &= 2\epsilon_u^n - \epsilon_u^{n-1}, & \bar{\epsilon}_\omega^n &= 2\epsilon_\omega^n - \epsilon_\omega^{n-1}, & \bar{\epsilon}_\theta^n &= 2\epsilon_\theta^n - \epsilon_\theta^{n-1}, \\ \bar{R}_{uh}^n &= 2R_{uh}^n - R_{uh}^{n-1}, & \bar{R}_{\omega h}^n &= 2R_{\omega h}^n - R_{\omega h}^{n-1}, & \bar{R}_{\theta h}^n &= 2R_{\theta h}^n - R_{\theta h}^{n-1}. \end{aligned}$$

Assumption (A.3) ([20, 28]). $\max(\|\epsilon_u^0\|_0, \|\epsilon_u^1\|_0, \|\epsilon_\omega^0\|_0, \|\epsilon_\omega^1\|_0, \|\epsilon_\theta^0\|_0, \|\epsilon_\theta^1\|_0) \leq Ch^{l+1}$, and $\|\epsilon_p^1\|_1 \leq C$.

Based on Assumptions (A.1)-(A.3), error estimates for the velocity field and the angular velocity field can be obtained.

4.1 The suboptimal error estimate

To establish optimal error estimates for the second-order pressure projection scheme, a suboptimal error estimate is first derived. This preliminary estimate serves as a key step towards obtaining optimal convergence results.

Theorem 4.1. *Suppose that Assumptions (A.1)-(A.3) hold. Then, the errors satisfy*

$$\begin{aligned}
& \|\epsilon_u^{N+1}\|_0^2 + \|2\epsilon_u^{N+1} - \epsilon_u^{N-1}\|_0^2 + \zeta \|\epsilon_\omega^{N+1}\|_0^2 + \zeta \|2\epsilon_\omega^{N+1} - \epsilon_\omega^{N-1}\|_0^2 + \|\epsilon_\theta^{N+1}\|_0^2 + \|2\epsilon_\theta^{N+1} - \epsilon_\theta^{N-1}\|_0^2 \\
& + \frac{8\delta_t^2}{3} \|\nabla \epsilon_p^{N+1}\|_0^2 + \sum_{n=0}^N \left((\chi + \mu) \delta_t \|\nabla \tilde{\epsilon}_u^{n+1}\|_0^2 + v \delta_t \|\nabla \epsilon_\omega^{n+1}\|_0^2 + \kappa \delta_t \|\nabla \epsilon_\theta^{n+1}\|_0^2 \right. \\
& + \|\epsilon_u^{n+1} - 2\epsilon_u^n + \epsilon_u^{n-1}\|_0^2 + \zeta \|\epsilon_\omega^{n+1} - 2\epsilon_\omega^n + \epsilon_\omega^{n-1}\|_0^2 + \|\epsilon_\theta^{n+1} - 2\epsilon_\theta^n + \epsilon_\theta^{n-1}\|_0^2 \\
& \left. + 6\|\tilde{\epsilon}_u^{n+1} - \epsilon_u^{n+1}\|_0^2 + 4\eta \delta_t \|\nabla \cdot \epsilon_\omega^{n+1}\|_0^2 + 16\chi \delta_t \|\epsilon_\omega^{n+1}\|_0^2 \right) \leq C(\delta_t^2 + h^{2l+2}), \tag{4.9}
\end{aligned}$$

where C is a positive number independent of δ_t and h .

Proof. Subtracting (4.5), (4.7), and (4.8) from (3.2), (3.5), and (3.6), respectively, we derive

$$\begin{aligned}
& \left(\frac{3\tilde{\epsilon}_u^{n+1} - 4\epsilon_u^n + \epsilon_u^{n-1}}{2\delta_t}, v_h \right) + (\chi + \mu)(\nabla \tilde{\epsilon}_u^{n+1}, \nabla v_h) + ((R_{uh}^{n+1} \cdot \nabla) R_{uh}^{n+1} - (\tilde{u}_h^n \cdot \nabla) \tilde{u}_h^{n+1}, v_h) \\
& + (\nabla Q_h^{n+1} - \nabla p_h^n, v_h) = 2\chi(\nabla \times R_{\omega h}^{n+1} - \nabla \times \tilde{\omega}_h^n, v_h) + (R_{\theta h}^{n+1} e - \tilde{\theta}_h^n e, v_h) + (R_{ul}^{n+1}, v_h), \tag{4.10}
\end{aligned}$$

$$\begin{aligned}
& \zeta \left(\frac{3\epsilon_\omega^{n+1} - 4\epsilon_\omega^n + \epsilon_\omega^{n-1}}{2\delta_t}, \Lambda_h \right) + v(\nabla \epsilon_\omega^{n+1}, \nabla \Lambda_h) + \zeta((R_{uh}^{n+1} \cdot \nabla) R_{\omega h}^{n+1} - (\tilde{u}_h^n \cdot \nabla) \omega_h^{n+1}, \Lambda_h) \\
& + \eta(\nabla \cdot \epsilon_\omega^{n+1}, \nabla \cdot \Lambda_h) + 4\chi(\epsilon_\omega^{n+1}, \Lambda_h) = 2\chi(\nabla \times R_{uh}^{n+1} - \nabla \times \tilde{u}_h^n, \Lambda_h) + (R_{\omega l}^{n+1}, \Lambda_h), \tag{4.11}
\end{aligned}$$

$$\begin{aligned}
& \left(\frac{3\epsilon_\theta^{n+1} - 4\epsilon_\theta^n + \epsilon_\theta^{n-1}}{2\delta_t}, \psi_h \right) + \kappa(\nabla \epsilon_\theta^{n+1}, \nabla \psi_h) + ((R_{uh}^{n+1} \cdot \nabla) R_{\theta h}^{n+1} - (\tilde{u}_h^n \cdot \nabla) \theta_h^{n+1}, \psi_h) \\
& = (R_{uh}^{n+1} \cdot e - \tilde{u}_h^n \cdot e, \psi_h) + (R_{\theta l}^{n+1}, \psi_h). \tag{4.12}
\end{aligned}$$

Testing (4.10), (4.11) and (4.12) by $4\delta_t \tilde{\epsilon}_u^{n+1}$, $4\delta_t \epsilon_\omega^{n+1}$ and $4\delta_t \epsilon_\theta^{n+1}$ respectively, we have

$$\begin{aligned}
& 2(3\tilde{\epsilon}_u^{n+1} - 4\epsilon_u^n + \epsilon_u^{n-1}, \tilde{\epsilon}_u^{n+1}) + 4(\chi + \mu) \delta_t \|\nabla \tilde{\epsilon}_u^{n+1}\|_0^2 \\
& + 4\delta_t((R_{uh}^{n+1} \cdot \nabla) R_{uh}^{n+1} - (\tilde{u}_h^n \cdot \nabla) \tilde{u}_h^{n+1}, \tilde{\epsilon}_u^{n+1}) + 4\delta_t(\nabla Q_h^{n+1} - \nabla p_h^n, \tilde{\epsilon}_u^{n+1}) \\
& = 8\chi \delta_t(\nabla \times R_{\omega h}^{n+1} - \nabla \times \tilde{\omega}_h^n, \tilde{\epsilon}_u^{n+1}) + 4\delta_t(R_{\theta h}^{n+1} e - \tilde{\theta}_h^n e, \tilde{\epsilon}_u^{n+1}) + 4\delta_t(R_{ul}^{n+1}, \tilde{\epsilon}_u^{n+1}), \tag{4.13}
\end{aligned}$$

$$\begin{aligned}
& 2\zeta(3\epsilon_\omega^{n+1} - 4\epsilon_\omega^n + \epsilon_\omega^{n-1}, \epsilon_\omega^{n+1}) + 4v \delta_t \|\nabla \epsilon_\omega^{n+1}\|_0^2 \\
& + 4\delta_t \zeta((R_{uh}^{n+1} \cdot \nabla) R_{\omega h}^{n+1} - (\tilde{u}_h^n \cdot \nabla) \omega_h^{n+1}, \epsilon_\omega^{n+1}) + 4\eta \delta_t \|\nabla \cdot \epsilon_\omega^{n+1}\|_0^2 + 16\chi \delta_t \|\epsilon_\omega^{n+1}\|_0^2 \\
& = 8\chi \delta_t(\nabla \times R_{uh}^{n+1} - \nabla \times \tilde{u}_h^n, \epsilon_\omega^{n+1}) + 4\delta_t(R_{\omega l}^{n+1}, \epsilon_\omega^{n+1}), \tag{4.14}
\end{aligned}$$

$$\begin{aligned}
& 2(3\epsilon_\theta^{n+1} - 4\epsilon_\theta^n + \epsilon_\theta^{n-1}, \epsilon_\theta^{n+1}) + 4\kappa \delta_t \|\nabla \epsilon_\theta^{n+1}\|_0^2 + 4\delta_t((R_{uh}^{n+1} \cdot \nabla) R_{\theta h}^{n+1} - (\tilde{u}_h^n \cdot \nabla) \theta_h^{n+1}, \epsilon_\theta^{n+1}) \\
& = 4\delta_t(R_{\theta h}^{n+1} - \tilde{\theta}_h^n e, \epsilon_\theta^{n+1}) + 4\delta_t(R_{\theta l}^{n+1}, \epsilon_\theta^{n+1}). \tag{4.15}
\end{aligned}$$

By adding and subtracting terms $u(t^{n+1}), \nabla Q_h^{n+1}$ and ∇Q_h^n in (3.4) to obtain

$$\frac{3(\tilde{\epsilon}_u^{n+1} - \epsilon_u^{n+1})}{2\delta_t} = \nabla \epsilon_p^{n+1} - \nabla \epsilon_p^n - \nabla Q_h^{n+1} + \nabla Q_h^n. \tag{4.16}$$

Testing (4.16) by $4\delta_t(\nabla\epsilon_p^n + \nabla Q_h^{n+1} - \nabla Q_h^n)$ to get

$$6(\nabla\epsilon_p^n + \nabla Q_h^{n+1} - \nabla Q_h^n, \tilde{\epsilon}_u^{n+1}) = 4\delta_t(\nabla\epsilon_p^{n+1} - \nabla\epsilon_p^n - \nabla Q_h^{n+1} + \nabla Q_h^n, \nabla\epsilon_p^{n+1}) - \frac{3}{2\delta_t}\|\tilde{\epsilon}_u^{n+1} - \epsilon_u^{n+1}\|_0^2. \quad (4.17)$$

Based on (4.17), it follows that

$$\begin{aligned} 4\delta_t(\nabla\epsilon_p^n + \nabla Q_h^{n+1} - \nabla Q_h^n, \tilde{\epsilon}_u^{n+1}) &= -6\|\tilde{\epsilon}_u^{n+1} - \epsilon_u^{n+1}\|_0^2 - \frac{8\delta_t^2}{3}(\nabla Q_h^{n+1} - \nabla Q_h^n, \nabla\epsilon_p^{n+1}) \\ &\quad + \frac{4\delta_t^2}{3}(\|\nabla\epsilon_p^{n+1}\|_0^2 - \|\nabla\epsilon_p^n\|_0^2 + \|\nabla\epsilon_p^{n+1} - \nabla\epsilon_p^n\|_0^2). \end{aligned} \quad (4.18)$$

The first term of (4.13) can be rewritten as

$$\begin{aligned} 2(3\tilde{\epsilon}_u^{n+1} - 4\epsilon_u^{n+1} + \epsilon_u^{n-1}, \tilde{\epsilon}_u^{n+1}) &= \|\epsilon_u^{n+1}\|_0^2 - \|\epsilon_u^n\|_0^2 + \|2\epsilon_u^{n+1} - \epsilon_u^n\|_0^2 - \|2\epsilon_u^n - \epsilon_u^{n-1}\|_0^2 \\ &\quad + \|\epsilon_u^{n+1} - 2\epsilon_u^n + \epsilon_u^{n-1}\|_0^2 + 6\|\tilde{\epsilon}_u^{n+1} - \epsilon_u^{n+1}\|_0^2. \end{aligned} \quad (4.19)$$

Using Hölder's inequality and Young's inequality, we get

$$\begin{aligned} &|-4\delta_t((R_{uh}^{n+1} \cdot \nabla)R_{uh}^{n+1} - (\tilde{u}_h^n \cdot \nabla)\tilde{u}_h^{n+1}, \tilde{\epsilon}_u^{n+1})| \\ &\leq C\delta_t\|2\epsilon_u^n - \epsilon_u^{n-1}\|_0^2 + C\delta_t^5 + (\chi + \mu)\|\nabla\tilde{\epsilon}_u^{n+1}\|_0^2. \end{aligned} \quad (4.20)$$

$$|8\chi\delta_t(\nabla \times R_{\omega h}^{n+1} - \nabla \times \tilde{\omega}_h^n, \tilde{\epsilon}_u^{n+1})| \leq C\delta_t\|2\epsilon_\omega^n - \epsilon_\omega^{n-1}\|_0^2 + C\delta_t^5 + (\chi + \mu)\delta_t\|\nabla\tilde{\epsilon}_u^{n+1}\|_0^2, \quad (4.21)$$

$$|4\delta_t(R_{\theta h}^{n+1}e - \tilde{\theta}_h^n e, \tilde{\epsilon}_u^{n+1})| \leq C\delta_t\|2\epsilon_\theta^n - \epsilon_\theta^{n-1}\|_0^2 + C\delta_t^5 + (\chi + \mu)\delta_t\|\nabla\tilde{\epsilon}_u^{n+1}\|_0^2, \quad (4.22)$$

$$|4\delta_t(R_{ul}^{n+1}, \tilde{\epsilon}_u^{n+1})| \leq C\delta_t(\delta_t^2 + h^{l+1})^2 + (\chi + \mu)\delta_t\|\nabla\tilde{\epsilon}_u^{n+1}\|_0^2, \quad (4.23)$$

$$\left| \frac{8\delta_t^2}{3}(\nabla Q_h^{n+1} - \nabla Q_h^n, \nabla\epsilon_p^{n+1}) \right| \leq \frac{4\delta_t}{3}\|\nabla Q_h^{n+1} - \nabla Q_h^n\|_0^2 + C\delta_t^3\|\nabla\epsilon_p^{n+1}\|_0^2, \quad (4.24)$$

$$|4\delta_t(R_{\omega l}^{n+1}, \epsilon_\omega^{n+1})| \leq C\delta_t\|R_{\omega l}^{n+1}\|_0^2 + \nu\delta_t\|\nabla\epsilon_\omega^{n+1}\|_0^2, \quad (4.25)$$

$$\begin{aligned} &|-4\delta_t\zeta((R_{uh}^{n+1} \cdot \nabla)R_{\omega h}^{n+1} - (\tilde{u}_h^n \cdot \nabla)\omega_h^{n+1}, \epsilon_\omega^{n+1})| \\ &\leq \nu\delta_t\|\nabla\epsilon_\omega^{n+1}\|_0^2 + C\delta_t\|2\epsilon_u^n - \epsilon_u^{n-1}\|_0^2 + C\delta_t\|R_{uh}^{n+1} - 2R_{uh}^n + R_{uh}^{n-1}\|_0^2, \end{aligned} \quad (4.26)$$

$$\begin{aligned} &|4\delta_t(R_{\theta h}^{n+1} - \tilde{\theta}_h^n e, \epsilon_\theta^{n+1})| \\ &\leq C\delta_t(\|2\epsilon_\theta^n - \epsilon_\theta^{n-1}\|_0^2 + \|R_{\theta h}^{n+1} - 2R_{\theta h}^n + R_{\theta h}^{n-1}\|_0^2) + \kappa\delta_t\|\nabla\epsilon_\theta^{n+1}\|_0^2, \end{aligned} \quad (4.27)$$

$$\begin{aligned} &|8\chi\delta_t(\nabla \times R_{uh}^{n+1} - \nabla \times \tilde{u}_h^n, \epsilon_\omega^{n+1})| \\ &\leq C\delta_t(\|2\epsilon_u^n - \epsilon_u^{n-1}\|_0^2 + \|R_{uh}^{n+1} - 2R_{uh}^n + R_{uh}^{n-1}\|_0^2) + \nu\delta_t\|\nabla\epsilon_\omega^{n+1}\|_0^2, \end{aligned} \quad (4.28)$$

$$\begin{aligned} &|4\delta_t((R_{uh}^{n+1} \cdot \nabla)R_{\theta h}^{n+1} - (\tilde{u}_h^n \cdot \nabla)\theta_h^{n+1}, \epsilon_\theta^{n+1})| \\ &\leq C\delta_t(\|2\epsilon_u^n - \epsilon_u^{n-1}\|_0^2 + \|R_{uh}^{n+1} - 2R_{uh}^n + R_{uh}^{n-1}\|_0^2) + \kappa\delta_t\|\nabla\epsilon_\theta^{n+1}\|_0^2, \end{aligned} \quad (4.29)$$

$$|4\delta_t(R_{\theta l}^{n+1}, \epsilon_\theta^{n+1})| \leq C\delta_t\|R_{\theta l}^{n+1}\|_0^2 + \kappa\delta_t\|\nabla\epsilon_\theta^{n+1}\|_0^2. \quad (4.30)$$

Combining (4.13)-(4.30) and summing up $n=1$ to N , we derive

$$\begin{aligned}
& \|\epsilon_u^{N+1}\|_0^2 + \|2\epsilon_u^{N+1} - \epsilon_u^N\|_0^2 + \zeta\|\epsilon_\omega^{N+1}\|_0^2 + \zeta\|2\epsilon_\omega^{N+1} - \epsilon_\omega^{N-1}\|_0^2 + \zeta\|\epsilon_\theta^{N+1}\|_0^2 + \|2\epsilon_\theta^{N+1} - \epsilon_\theta^{N-1}\|_0^2 \\
& + \delta_t \sum_{n=0}^N ((\chi + \mu)\|\nabla \tilde{\epsilon}_u^{n+1}\|_0^2 + v\|\nabla \epsilon_\omega^{n+1}\|_0^2 + \kappa\|\nabla \epsilon_\theta^{n+1}\|_0^2) + \sum_{n=0}^N (\|\epsilon_u^{n+1} - 2\epsilon_u^n + \epsilon_u^{n-1}\|_0^2 \\
& + \|\epsilon_\omega^{n+1} - 2\epsilon_\omega^n + \epsilon_\omega^{n-1}\|_0^2 + \|\epsilon_\theta^{n+1} - 2\epsilon_\theta^n + \epsilon_\theta^{n-1}\|_0^2 + 6\|\tilde{\epsilon}_u^{n+1} - \epsilon_u^{n+1}\|_0^2) + \frac{8\delta_t^2}{3}\|\nabla \epsilon_p^{N+1}\|_0^2 \\
& \leq \|\epsilon_u^0\|_0^2 + \|2\epsilon_u^1 - \epsilon_u^0\|_0^2 + \zeta\|\epsilon_\omega^0\|_0^2 + \zeta\|2\epsilon_\omega^1 - \epsilon_\omega^0\|_0^2 + \|\epsilon_\theta^1\|_0^2 + \|2\epsilon_\theta^1 - \epsilon_\theta^0\|_0^2 \\
& + C(\sum_{n=1}^{N+1} \|2\epsilon_u^n - \epsilon_u^{n-1}\|_0^2 + \sum_{n=1}^{N+1} \zeta\|2\epsilon_\omega^n - \epsilon_\omega^{n-1}\|_0^2 + \sum_{n=1}^{N+1} \|2\epsilon_\theta^n - \epsilon_\theta^{n-1}\|_0^2 + \sum_{n=1}^{N+1} \|R_{ul}^{n+1}\|_0^2 \\
& + \sum_{n=1}^{N+1} \|R_{\omega l}^{n+1}\|_0^2 + \sum_{n=1}^{N+1} \|R_{\theta l}^{n+1}\|_0^2 + \sum_{n=1}^{N+1} \delta_t \|R_{\theta h}^{n+1} - 2R_{\theta h}^n + R_{\theta h}^{n-1}\|_0^2 + \delta_t \|R_{uh}^{n+1} - 2R_{uh}^n + R_{uh}^{n-1}\|_0^2 \\
& + \delta_t \|R_{\omega h}^{n+1} - 2R_{\omega h}^n + R_{\omega h}^{n-1}\|_0^2 + \frac{16}{3}\delta_t \sum_{n=1}^{N+1} \|\nabla Q_h^{n+1} - \nabla Q_h^n\|_0^2 + \delta_t^2 \sum_{n=1}^{N+1} \|\nabla \epsilon_p^{n+1}\|_0^2), \quad (4.31)
\end{aligned}$$

where we have used the following estimations [20, 40, 41]

$$\begin{aligned}
& \|\nabla(Q_h^{n+1} - Q_h^n)\|_0 \leq C\delta_t, \quad \|R_{uh}^{n+1} - 2R_{uh}^n + R_{uh}^{n-1}\|_0 \leq C\delta_t^2, \quad \|R_{\omega h}^{n+1} - 2R_{\omega h}^n + R_{\omega h}^{n-1}\|_0 \leq C\delta_t^2, \\
& \|R_{\theta h}^{n+1} - 2R_{\theta h}^n + R_{\theta h}^{n-1}\|_0 \leq C\delta_t^2, \quad \|R_{ul}^{n+1}\|_0 + \|R_{\omega l}^{n+1}\|_0 + \|R_{\theta l}^{n+1}\|_0 \leq C(\delta_t^2 + h^{l+1}).
\end{aligned}$$

By Assumption(A.3) and Grönwall's lemma, the proof is completed. \square

Suboptimal error estimates indicate that the pressure term causes the loss of optimal convergence, thereby reducing the overall accuracy. To address this issue, the dual-norm technique is introduced. The appropriate operators and associated dual norms are then defined to recover the optimal error estimate and eliminate pressure-induced order reduction.

4.2 The optimal error estimate

We define the inverse Stokes operator \mathcal{A}^{-1} [27, 28, 41] as follows.

$$\mathcal{A}^{-1}: V_1^{-1}(\Omega)^d \rightarrow V, \quad \forall v \in V_1^{-1}(\Omega)^d, \mathcal{A}^{-1}(v) \in V,$$

which satisfies the following problem:

$$\begin{cases} (\nabla \mathcal{A}^{-1}(v), \nabla w) - (r, \nabla \cdot w) = (v, w), & \forall w \in H_0^1(\Omega)^d, \\ (r, \nabla \cdot \mathcal{A}^{-1}(v)) = 0, & \forall q \in L_0^2(\Omega), \end{cases}$$

where (\cdot, \cdot) denotes the duality pairing between $H^{-1}(\Omega)^d$ and $H^1(\Omega)^d$. It follows that

$$\|\mathcal{A}^{-1}(v)\|_1 + \|\nabla r\|_0 \leq C\|v\|_{-1}, \quad \forall v \in H^{-1}(\Omega)^d. \quad (4.32)$$

If the boundary $\partial\Omega$ is sufficiently smooth, the following regularity estimate holds [38]:

$$\|\mathcal{A}^{-1}(\boldsymbol{v})\|_2 + \|\nabla r\|_0 \leq C\|\boldsymbol{v}\|_0, \quad \forall \boldsymbol{v} \in L^2(\Omega)^d. \quad (4.33)$$

The bilinear form [28]

$$H^{-1}(\Omega)^d \times H^{-1}(\Omega)^d \ni (\boldsymbol{v}, \boldsymbol{w}) \mapsto (\mathcal{A}^{-1}(\boldsymbol{v}), \boldsymbol{w}) := (\nabla \mathcal{A}^{-1}(\boldsymbol{v}), \nabla \mathcal{A}^{-1}(\boldsymbol{w})) \in \mathbb{R}$$

induces a semi-norm in $H^{-1}(\Omega)^d$, denoted by $|\cdot|_*$, defined as

$$|\boldsymbol{v}|_* = \|\nabla \mathcal{A}^{-1}(\boldsymbol{v})\|_0 \leq C\|\boldsymbol{v}\|_{-1}, \quad \forall \boldsymbol{v} \in H^{-1}(\Omega)^d. \quad (4.34)$$

Similarly, the inverse elliptic operator $\tilde{\mathcal{A}}^{-1}$ [42] is defined as $\tilde{\mathcal{A}}^{-1}: H^{-1}(\Omega)^d \rightarrow \mathbf{X}$, where for any $\boldsymbol{w} \in H^{-1}(\Omega)^d$, the function $\tilde{\mathcal{A}}^{-1}(\boldsymbol{w}) \in \mathbf{X}$ satisfies

$$(\nabla \tilde{\mathcal{A}}^{-1}(\boldsymbol{w}), \nabla \boldsymbol{v}) = (\boldsymbol{w}, \boldsymbol{v}), \quad \forall \boldsymbol{v} \in H_0^1(\Omega)^d. \quad (4.35)$$

Then

$$\|\tilde{\mathcal{A}}^{-1}(\boldsymbol{w})\|_1 \leq C\|\boldsymbol{w}\|_{-1}, \quad \forall \boldsymbol{w} \in H^{-1}(\Omega)^d. \quad (4.36)$$

If the domain Ω is sufficiently smooth, the regularity property will be activated

$$\|\tilde{\mathcal{A}}^{-1}(\boldsymbol{w})\|_2 \leq C\|\boldsymbol{w}\|_0, \quad \forall \boldsymbol{w} \in L^2(\Omega)^d \quad (4.37)$$

holds. Following [28], the bilinear form

$$H^{-1}(\Omega)^d \times H^{-1}(\Omega)^d \ni (\boldsymbol{v}, \boldsymbol{w}) \mapsto (\tilde{\mathcal{A}}^{-1}(\boldsymbol{v}), \boldsymbol{w}) := (\nabla \tilde{\mathcal{A}}^{-1}(\boldsymbol{v}), \nabla \tilde{\mathcal{A}}^{-1}(\boldsymbol{w})) \in \mathbb{R}$$

induces a semi-norm on $H^{-1}(\Omega)^d$, denoted by $|\cdot|_*$, satisfying

$$|\boldsymbol{w}|_* = \|\nabla \tilde{\mathcal{A}}^{-1}(\boldsymbol{w})\|_0 \leq C\|\boldsymbol{w}\|_{-1}, \quad \forall \boldsymbol{w} \in H^{-1}(\Omega)^d. \quad (4.38)$$

Theorem 4.2. *Suppose that Assumptions (A.1)-(A.3) are satisfied. The following optimal error estimates hold*

$$\begin{aligned} & |\epsilon_u^{N+1}|_*^2 + |2\epsilon_u^{N+1} - \epsilon_u^N|_*^2 + \zeta|\epsilon_\omega^{N+1}|_*^2 + \zeta|2\epsilon_\omega^{N+1} - \epsilon_\omega^{N-1}|_*^2 + |\epsilon_\theta^{N+1}|_*^2 + |2\epsilon_\theta^{N+1} - \epsilon_\theta^{N-1}|_*^2 \\ & + \delta_t \sum_{n=0}^N \left(\frac{\chi + \mu}{2} \|\epsilon_u^{n+1}\|_0^2 + 4\nu \|\epsilon_\omega^{n+1}\|_0^2 + 4\eta \|\epsilon_\omega^{n+1}\|_0^2 + 16\chi \|\epsilon_\omega^{n+1}\|_0^2 + \frac{\kappa}{2} \|\epsilon_\theta^{n+1}\|_0^2 \right. \\ & \left. + |\epsilon_u^{n+1} - 2\epsilon_u^n + \epsilon_u^{n-1}|_*^2 + \zeta|\epsilon_\omega^{n+1} - 2\epsilon_\omega^n + \epsilon_\omega^{n-1}|_*^2 + |\epsilon_\theta^{n+1} - 2\epsilon_\theta^n + \epsilon_\theta^{n-1}|_*^2 \right) \leq C(\delta_t^2 + h^{l+1})^2. \end{aligned} \quad (4.39)$$

Proof. Testing (4.10), (4.11) and (4.12) by $4\delta_t \mathcal{A}^{-1} \tilde{\epsilon}_u^{n+1}$, $4\delta_t \tilde{\mathcal{A}}^{-1} \epsilon_\omega^{n+1}$, and $4\delta_t \tilde{\mathcal{A}}^{-1} \epsilon_\theta^{n+1}$, respectively, we have

$$\begin{aligned} & 2(3\tilde{\epsilon}_u^{n+1} - 4\epsilon_u^n + \epsilon_u^{n-1}, \mathcal{A}^{-1} \tilde{\epsilon}_{uu}^{n+1}) + 4(\chi + \mu) \delta_t (\nabla \tilde{\epsilon}_u^{n+1}, \nabla \mathcal{A}^{-1} \tilde{\epsilon}_u^{n+1}) + 4\delta_t ((R_{uh}^{n+1} \cdot \nabla) R_{uh}^{n+1} \\ & - (\bar{u}_h^n \cdot \nabla) \bar{u}_h^{n+1}, \mathcal{A}^{-1} \tilde{\epsilon}_u^{n+1}) + 4\delta_t (\nabla Q_h^{n+1} - \nabla p_h^n, \mathcal{A}^{-1} \tilde{\epsilon}_u^{n+1}) \\ & = 4\chi \delta_t (\nabla \times R_{\omega h}^{n+1} - \nabla \times \bar{\omega}_h^n, \mathcal{A}^{-1} \tilde{\epsilon}_u^{n+1}) + 4\delta_t (R_{\theta h}^{n+1} e - \bar{\theta}_h^n e, \mathcal{A}^{-1} \tilde{\epsilon}_u^{n+1}) + 4\delta_t (R_{ul}^{n+1}, \mathcal{A}^{-1} \tilde{\epsilon}_u^{n+1}), \end{aligned} \quad (4.40)$$

$$\begin{aligned} & \zeta |\epsilon_\omega^{n+1}|_* - \zeta |\epsilon_\omega^n|_* + \zeta |2\epsilon_\omega^{n+1} - \epsilon_\omega^n|_* - \zeta |2\epsilon_\omega^n - \epsilon_\omega^{n-1}|_* + \zeta |\epsilon_\omega^{n+1} - 2\epsilon_\omega^n + \epsilon_\omega^{n-1}|_* + 4\nu \delta_t \|\epsilon_\omega^{n+1}\|_0^2 \\ & + 4\delta_t \zeta ((R_{uh}^{n+1} \cdot \nabla) R_{\omega h}^{n+1} - (\bar{u}_h^n \cdot \nabla) \omega_h^{n+1}, \tilde{\mathcal{A}}^{-1} \epsilon_\omega^{n+1}) + 4\eta \delta_t \|\epsilon_\omega^{n+1}\|_0^2 + 16\chi \delta_t \|\epsilon_\omega^{n+1}\|_0^2 \\ & = 8\chi \delta_t (\nabla \times R_{uh}^{n+1} - \nabla \times \bar{u}_h^n, \tilde{\mathcal{A}}^{-1} \epsilon_\omega^{n+1}) + 4\delta_t (R_{\omega l}^{n+1}, \tilde{\mathcal{A}}^{-1} \epsilon_\omega^{n+1}), \end{aligned} \quad (4.41)$$

$$\begin{aligned} & |\epsilon_\theta^{n+1}|_* - |\epsilon_\theta^n|_* + |2\epsilon_\theta^{n+1} - \epsilon_\theta^n|_* - |2\epsilon_\theta^n - \epsilon_\theta^{n-1}|_* + |\epsilon_\theta^{n+1} - 2\epsilon_\theta^n + \epsilon_\theta^{n-1}|_* + 4\kappa \delta_t \|\epsilon_\theta^{n+1}\|_0^2 \\ & = -4\delta_t ((R_{uh}^{n+1} \cdot \nabla) R_{\theta h}^{n+1} - (\bar{u}_h^n \cdot \nabla) \theta_h^{n+1}, \tilde{\mathcal{A}}^{-1} \epsilon_\theta^{n+1}) + 4\delta_t (R_{\theta h}^{n+1} - \bar{\theta}_h^n e, \tilde{\mathcal{A}}^{-1} \epsilon_\theta^{n+1}) \\ & + 4\delta_t (R_{\theta l}^{n+1}, \tilde{\mathcal{A}}^{-1} \epsilon_\theta^{n+1}). \end{aligned} \quad (4.42)$$

The combination of (3.3), (4.2) and (4.34) yields

$$\begin{aligned} & 2(3\tilde{\epsilon}_u^{n+1} - 4\epsilon_u^n + \epsilon_u^{n-1}, \mathcal{A}^{-1} \tilde{\epsilon}_u^{n+1}) = 2(3\epsilon_u^{n+1} - 4\epsilon_u^n + \epsilon_u^{n-1}, \mathcal{A}^{-1} \tilde{\epsilon}_u^{n+1}) \\ & = |\epsilon_u^{n+1}|_*^2 - |\epsilon_u^n|_*^2 + |2\epsilon_u^{n+1} - \epsilon_u^n|_*^2 - |2\epsilon_u^n - \epsilon_u^{n-1}|_*^2 + |\epsilon_u^{n+1} - 2\epsilon_u^n + \epsilon_u^{n-1}|_*^2. \end{aligned} \quad (4.43)$$

$$4(\chi + \mu) \delta_t (\nabla \tilde{\epsilon}_u^{n+1}, \nabla \mathcal{A}^{-1} \tilde{\epsilon}_u^{n+1}) = 4(\chi + \mu) \delta_t (\tilde{\epsilon}_u^{n+1}, \tilde{\epsilon}_u^{n+1}) = 4(\chi + \mu) \delta_t \|\tilde{\epsilon}_u^{n+1}\|_0^2. \quad (4.44)$$

Using Hölder's inequality, Young's inequality, (4.33), (4.34), (4.37) and (4.38), we get

$$\begin{aligned} & |8\chi \delta_t (\nabla \times R_{\omega h}^{n+1} - \nabla \times \bar{\omega}_h^n, \mathcal{A}^{-1} \tilde{\epsilon}_u^{n+1})| \\ & = |8\chi \delta_t (\nabla \times \bar{R}_{\omega h}^n - \nabla \times \bar{\omega}_h^n, \mathcal{A}^{-1} \tilde{\epsilon}_u^{n+1}) + 8\chi \delta_t (\nabla \times (R_{\omega h}^{n+1} - 2R_{\omega h}^n + R_{\omega h}^{n-1}), \mathcal{A}^{-1} \tilde{\epsilon}_u^{n+1})| \\ & \leq C\delta_t |2\epsilon_\omega^n - \epsilon_\omega^{n-1}|_* \|\nabla \mathcal{A}^{-1} \tilde{\epsilon}_u^{n+1}\|_1 + C\delta_t \|R_{\omega h}^{n+1} - 2R_{\omega h}^n + R_{\omega h}^{n-1}\|_0 \|\nabla \mathcal{A}^{-1} \tilde{\epsilon}_u^{n+1}\|_0 \\ & \leq C\delta_t |\bar{\epsilon}_\omega^n|_*^2 + C\delta_t^5 + \frac{\chi + \mu}{2} \delta_t \|\tilde{\epsilon}_u^{n+1}\|_0^2, \end{aligned} \quad (4.45)$$

$$\begin{aligned} & |4\delta_t (R_{ul}^{n+1}, \mathcal{A}^{-1} \tilde{\epsilon}_u^{n+1})| \leq 4\delta_t \|R_{ul}^{n+1}\|_0 \|\mathcal{A}^{-1} \tilde{\epsilon}_u^{n+1}\|_0 \\ & \leq C\delta_t \|R_{ul}^{n+1}\|_0^2 + \frac{(\chi + \mu)}{2} \delta_t \|\nabla \mathcal{A}^{-1} \tilde{\epsilon}_u^{n+1}\|_0^2 \leq C\delta_t (\delta_t^2 + h^{l+1})^2 + \frac{(\chi + \mu)}{2} \delta_t \|\tilde{\epsilon}_u^{n+1}\|_0^2, \end{aligned} \quad (4.46)$$

$$\begin{aligned} & |4\delta_t (R_{\theta h}^{n+1} e - \bar{\theta}_h^n e, \mathcal{A}^{-1} \tilde{\epsilon}_u^{n+1})| = |4\delta_t (\bar{R}_{\theta h}^n e - \bar{\theta}_h^n e, \mathcal{A}^{-1} \tilde{\epsilon}_u^{n+1}) + 4\delta_t ((R_{\theta h}^{n+1} - 2R_{\theta h}^n + R_{\theta h}^{n-1}) e, \mathcal{A}^{-1} \tilde{\epsilon}_u^{n+1})| \\ & \leq 4\delta_t |\bar{\epsilon}_\theta^n|_* \|\nabla \mathcal{A}^{-1} \tilde{\epsilon}_u^{n+1}\|_0 + 4\delta_t \|R_{\theta h}^{n+1} - 2R_{\theta h}^n + R_{\theta h}^{n-1}\|_0 \|\nabla \mathcal{A}^{-1} \tilde{\epsilon}_u^{n+1}\|_0 \\ & \leq C\delta_t |\bar{\epsilon}_\theta^n|_*^2 + C\delta_t^5 + \frac{\chi + \mu}{2} \delta_t \|\tilde{\epsilon}_u^{n+1}\|_0^2, \end{aligned} \quad (4.47)$$

$$\begin{aligned}
& |-4\delta_t((R_{uh}^{n+1} \cdot \nabla)R_{uh}^{n+1} - (\bar{u}_h^n \cdot \nabla)\tilde{u}_h^{n+1}, \mathcal{A}^{-1}\tilde{\epsilon}_u^{n+1})| \\
& = |4\delta_t(((2\epsilon_u^n - \epsilon_u^{n-1}) \cdot \nabla)R_{uh}^{n+1}, \mathcal{A}^{-1}\tilde{\epsilon}_u^{n+1}) + 4\delta_t(((R_{uh}^{n+1} - 2R_{uh}^n + R_{uh}^{n-1}) \cdot \nabla)R_{uh}^{n+1}, \mathcal{A}^{-1}\tilde{\epsilon}_u^{n+1}) \\
& \quad + 4\delta_t(\bar{u}_h^n \cdot \nabla)\tilde{\epsilon}_u^{n+1}, \mathcal{A}^{-1}\tilde{\epsilon}_u^{n+1}) + 4\delta_t(((2\epsilon_u^n - \epsilon_u^{n-1}) \cdot \nabla)\tilde{\epsilon}_u^{n+1}, \mathcal{A}^{-1}\tilde{\epsilon}_u^{n+1})| \\
& \quad + 4\delta_t(((R_{uh}^{n+1} - 2R_{uh}^n + R_{uh}^{n-1}) \cdot \nabla)\tilde{u}_h^{n+1}, \mathcal{A}^{-1}\tilde{\epsilon}_u^{n+1}) \\
& \leq C\delta_t|\tilde{\epsilon}_u^n|_*^2 + C\delta_t\|R_{uh}^{n+1} - 2R_{uh}^n + R_{uh}^{n-1}\|_0^2 + \frac{\chi+\mu}{2}\delta_t\|\nabla\mathcal{A}^{-1}\tilde{\epsilon}_u^{n+1}\|_0^2 \\
& \quad + C\delta_t(\|R_{uh}^{n+1} - 2R_{uh}^n + R_{uh}^{n-1}\|_0^2 + \|\epsilon_u^n\|_0^2 + \|\epsilon_u^{n-1}\|_0^2)\|\nabla\tilde{\epsilon}_u^{n+1}\|_0^2 + C\delta_t(\|\epsilon_u^n\|_0^2 + \|\epsilon_u^{n-1}\|_0^2)\|\nabla\tilde{\epsilon}_u^{n+1}\|_0^2 \\
& \leq C\delta_t|\tilde{\epsilon}_u^n|_*^2 + C\delta_t^5 + C\delta_t(\delta_t^2 + h^{2l+2})\|\nabla\tilde{\epsilon}_u^{n+1}\|_0^2 + \frac{\chi+\mu}{2}\delta_t\|\tilde{\epsilon}_u^{n+1}\|_0^2, \tag{4.48}
\end{aligned}$$

$$\begin{aligned}
& |-4\delta_t\zeta((R_{\omega h}^{n+1} \cdot \nabla)R_{\omega h}^{n+1} - (\bar{u}_h^n \cdot \nabla)\omega_h^{n+1}, \tilde{\mathcal{A}}^{-1}\epsilon_\omega^{n+1})| \\
& = |-4\delta_t\zeta((\bar{\epsilon}_u^n \cdot \nabla)R_{\omega h}^{n+1}, \tilde{\mathcal{A}}^{-1}\epsilon_\omega^{n+1}) - 4\delta_t\zeta(((R_{uh}^{n+1} - 2R_{uh}^n + R_{uh}^{n-1}) \cdot \nabla)R_{\omega h}^{n+1}, \tilde{\mathcal{A}}^{-1}\epsilon_\omega^{n+1}) \\
& \quad - 4\delta_t\zeta((\bar{\epsilon}_u^n \cdot \nabla)\epsilon_\omega^{n+1}, \tilde{\mathcal{A}}^{-1}\epsilon_\omega^{n+1}) - 4\delta_t\zeta(((R_{uh}^{n+1} - 2R_{uh}^n + R_{uh}^{n-1}) \cdot \nabla)\epsilon_\omega^{n+1}, \tilde{\mathcal{A}}^{-1}\epsilon_\omega^{n+1})| \\
& \leq C\delta_t\zeta\|\bar{\epsilon}_u^n\|_0\|R_{\omega h}^{n+1}\|_{L^\infty}\|\nabla\tilde{\mathcal{A}}^{-1}\epsilon_\omega^{n+1}\|_0 + 4\delta_t\zeta\|R_{uh}^{n+1} - 2R_{uh}^n + R_{uh}^{n-1}\|_0\|R_{\omega h}^{n+1}\|_{L^\infty}\|\nabla\tilde{\mathcal{A}}^{-1}\epsilon_\omega^{n+1}\|_0 \\
& \quad + C\delta_t\zeta\|\bar{\epsilon}_u^n\|_0\|\nabla\epsilon_\omega^{n+1}\|_0\|\tilde{\mathcal{A}}^{-1}\epsilon_\omega^{n+1}\|_2 + 4\delta_t\zeta\|R_{uh}^{n+1} - 2R_{uh}^n + R_{uh}^{n-1}\|_0\|\nabla\epsilon_\omega^{n+1}\|_0\|\tilde{\mathcal{A}}^{-1}\epsilon_\omega^{n+1}\|_2 \\
& \leq \frac{\chi+\mu}{4}\delta_t(\|\epsilon_u^n\|_0^2 + \|\epsilon_u^{n-1}\|_0^2) + C\delta_t^5 + C\delta_t(\delta_t^2 + h^{2l+2})\|\nabla\epsilon_\omega^{n+1}\|_0^2 + C\delta_t|\epsilon_\omega^{n+1}|_*^2, \tag{4.49}
\end{aligned}$$

$$\begin{aligned}
& |8\chi\delta_t(\nabla \times R_{uh}^{n+1} - \nabla \times \bar{u}_h^n, \tilde{\mathcal{A}}^{-1}\epsilon_\omega^{n+1})| \\
& = |8\chi\delta_t(\nabla \times \bar{R}_{uh}^n - \nabla \times \bar{u}_h^n, \tilde{\mathcal{A}}^{-1}\epsilon_\omega^{n+1}) + 8\chi\delta_t(\nabla \times (R_{uh}^{n+1} - 2R_{uh}^n + R_{uh}^{n-1}), \tilde{\mathcal{A}}^{-1}\epsilon_\omega^{n+1})| \\
& \leq C\delta_t(\|\epsilon_u^n\|_0 + \|\epsilon_u^{n-1}\|_0)\|\nabla\tilde{\mathcal{A}}^{-1}\epsilon_\omega^{n+1}\|_0 + C\delta_t\|R_{uh}^{n+1} - 2R_{uh}^n + R_{uh}^{n-1}\|_0\|\nabla\tilde{\mathcal{A}}^{-1}\epsilon_\omega^{n+1}\|_0 \\
& \leq \frac{\chi+\mu}{4}\delta_t(\|\epsilon_u^n\|_0^2 + \|\epsilon_u^{n-1}\|_0^2) + C\delta_t^5 + C\delta_t|\epsilon_\omega^{n+1}|_*^2, \tag{4.50}
\end{aligned}$$

$$\begin{aligned}
& |4\delta_t(R_{\omega l}^{n+1}, \tilde{\mathcal{A}}^{-1}\epsilon_\omega^{n+1})| \leq 4\delta_t\|R_{\omega l}^{n+1}\|_0\|\tilde{\mathcal{A}}^{-1}\epsilon_\omega^{n+1}\|_0 \leq C\delta_t\|R_{\omega l}^{n+1}\|_0^2 + v\delta_t\|\nabla\tilde{\mathcal{A}}^{-1}\epsilon_\omega^{n+1}\|_0^2 \\
& \leq C\delta_t\|R_{\omega l}^{n+1}\|_0^2 + v\delta_t|\epsilon_\omega^{n+1}|_*^2 \leq C\delta_t(\delta_t^2 + h^{l+1})^2 + v\delta_t|\epsilon_\omega^{n+1}|_*^2, \tag{4.51}
\end{aligned}$$

$$\begin{aligned}
& |4\delta_t((R_{\theta h}^{n+1} \cdot \nabla)R_{\theta h}^{n+1} - (\bar{u}_h^n \cdot \nabla)\theta_h^{n+1}, \tilde{\mathcal{A}}^{-1}\epsilon_\theta^{n+1})| \\
& = |4\delta_t((\bar{\epsilon}_u^n \cdot \nabla)R_{\theta h}^{n+1}, \tilde{\mathcal{A}}^{-1}\epsilon_\theta^{n+1}) + 4\delta_t(((R_{uh}^{n+1} - 2R_{uh}^n + R_{uh}^{n-1}) \cdot \nabla)R_{\theta h}^{n+1}, \tilde{\mathcal{A}}^{-1}\epsilon_\theta^{n+1}) \\
& \quad + 4\delta_t((\bar{\epsilon}_u^n \cdot \nabla)\epsilon_\theta^{n+1}, \tilde{\mathcal{A}}^{-1}\epsilon_\theta^{n+1}) + 4\delta_t(((R_{uh}^{n+1} - 2R_{uh}^n + R_{uh}^{n-1}) \cdot \nabla)\epsilon_\theta^{n+1}, \tilde{\mathcal{A}}^{-1}\epsilon_\theta^{n+1})| \\
& \leq 4\delta_t\|\bar{\epsilon}_u^n\|_0\|R_{\theta h}^{n+1}\|_{L^\infty}\|\nabla\tilde{\mathcal{A}}^{-1}\epsilon_\theta^{n+1}\|_0 + 4\delta_t\|R_{uh}^{n+1} - 2R_{uh}^n + R_{uh}^{n-1}\|_0\|R_{\theta h}^{n+1}\|_{L^\infty}\|\nabla\tilde{\mathcal{A}}^{-1}\epsilon_\theta^{n+1}\|_0 \\
& \quad + 4\delta_t\|\bar{\epsilon}_u^n\|_0\|\nabla\epsilon_\theta^{n+1}\|_0\|\tilde{\mathcal{A}}^{-1}\epsilon_\theta^{n+1}\|_2 + 4\delta_t\|R_{uh}^{n+1} - 2R_{uh}^n + R_{uh}^{n-1}\|_0\|\nabla\epsilon_\theta^{n+1}\|_0\|\tilde{\mathcal{A}}^{-1}\epsilon_\theta^{n+1}\|_2 \\
& \leq \frac{\chi+\mu}{4}\delta_t(\|\epsilon_u^n\|_0^2 + \|\epsilon_u^{n-1}\|_0^2) + C\delta_t^5 + C\delta_t(\delta_t^2 + h^{2l+2})\|\nabla\epsilon_\theta^{n+1}\|_0^2 + C\delta_t|\epsilon_\theta^{n+1}|_*^2. \tag{4.52}
\end{aligned}$$

$$\begin{aligned}
& |4\delta_t(R_{\theta h}^{n+1} - \bar{\theta}_h^n e, \tilde{\mathcal{A}}^{-1}\epsilon_\theta^{n+1})| \\
& \leq 4\delta_t(2\|\epsilon_\theta^n\|_0 + \|\epsilon_\theta^{n-1}\|_0)\|\tilde{\mathcal{A}}^{-1}\epsilon_\theta^{n+1}\|_0 + 4\delta_t\|R_{\theta h}^{n+1} - 2R_{\theta h}^n + R_{\theta h}^{n-1}\|_0\|\tilde{\mathcal{A}}^{-1}\epsilon_\theta^{n+1}\|_0 \\
& \leq \frac{7\kappa\delta_t}{4}(\|\epsilon_\theta^n\|_0^2 + \|\epsilon_\theta^{n-1}\|_0^2) + C\delta_t^5 + C\delta_t|\epsilon_\theta^{n+1}|_*^2. \tag{4.53}
\end{aligned}$$

$$\begin{aligned}
& \frac{\chi+\mu}{2}\delta_t\|\tilde{\epsilon}_u^{n+1}\|_0^2 = \frac{\chi+\mu}{2}\delta_t\|\epsilon_u^{n+1}\|_0^2 + \frac{2(\chi+\mu)\delta_t^3}{9}\|\nabla(\epsilon_p^{n+1} - \epsilon_p^n)\|_0^2 + \frac{2(\chi+\mu)\delta_t^3}{9}\|\nabla(Q_h^{n+1} - Q_h^n)\|_0^2. \tag{4.54}
\end{aligned}$$

Combining (4.40)-(4.54) and summing up from $n = 1$ to N , we derive

$$\begin{aligned}
& \|\epsilon_u^{N+1}\|_0^2 + \|2\epsilon_u^{N+1} - \epsilon_u^N\|_0^2 + |\epsilon_\omega^{N+1}|_*^2 + |2\epsilon_\omega^{N+1} - \epsilon_\omega^{N-1}|_*^2 + |\epsilon_\theta^{N+1}|_*^2 + |2\epsilon_\theta^{N+1} - \epsilon_\theta^{N-1}|_*^2 \\
& + \delta_t \sum_{n=0}^N \left(\frac{\chi + \mu}{2} \|\epsilon_u^{n+1}\|_0^2 + \nu \|\epsilon_\omega^{n+1}\|_0^2 + 4\eta \|\epsilon_\omega^{n+1}\|_0^2 + 16\chi \|\epsilon_\omega^{n+1}\|_0^2 + \frac{\kappa}{2} \|\epsilon_\theta^{n+1}\|_0^2 \right. \\
& \left. + |\epsilon_u^{n+1} - 2\epsilon_u^n + \epsilon_u^{n-1}|_*^2 + |\epsilon_\omega^{n+1} - 2\epsilon_\omega^n + \epsilon_\omega^{n-1}|_*^2 + |\epsilon_\theta^{n+1} - 2\epsilon_\theta^n + \epsilon_\theta^{n-1}|_*^2 \right) \\
& \leq \|\epsilon_u^1\|_0^2 + \|2\epsilon_u^1 - \epsilon_u^0\|_0^2 + |\epsilon_\omega^1|_*^2 + |2\epsilon_\omega^1 - \epsilon_\omega^0|_*^2 + |\epsilon_\theta^1|_*^2 + |2\epsilon_\theta^1 - \epsilon_\theta^0|_*^2 + C\delta_t (\|\epsilon_u^0\|_0^2 + \|\epsilon_u^1\|_0^2 + \|\epsilon_\omega^0\|_0^2 \\
& + \|\epsilon_\omega^1\|_0^2 + \|\epsilon_\theta^0\|_0^2 + \|\epsilon_\theta^1\|_0^2) + C\delta_t (\delta_t^2 + h^{l+1})^2 + C\delta_t \left(\sum_{n=1}^{N+1} (|\bar{\epsilon}_u^n|_*^2 + |\epsilon_\theta^{n+1}|_*^2 + |\epsilon_\omega^{n+1}|_*^2) \right).
\end{aligned}$$

By Assumption(A.3) and Grönwall's lemma, we complete the proof. \square

5 Numerical examples

In this section, we conduct several 2D and 3D numerical simulations to verify the accuracy and stability of the second-order pressure projection method for the micropolar Rayleigh-Bénard convection system and illustrate interesting phenomena in benchmark problems. The implementation of our codes is based on the open source element method software *Freefem++* [43].

5.1 Accuracy tests in 2D

We examine the two-dimensional micropolar Rayleigh-Bénard convection system with $\Omega = (0,1)^2$ satisfying the exact solution:

$$\begin{cases} \mathbf{u} = (\sin(2\pi x + t) \sin(2\pi y + t), \cos(2\pi x + t) \cos(2\pi y + t)), \\ p = \sin(2\pi(x - y) + t), \\ \omega = \sin(2\pi x + t) \sin(2\pi y + t), \\ \theta = \cos(2\pi x + t) \cos(2\pi y + t). \end{cases}$$

The finite element spaces are selected as $P2 - P1 - P2 - P2$ finite element spaces which satisfy the Ladyzhenskaya-Babuška-Brezzi condition. To achieve the optimal convergence rate, we set $\delta_t = h^{\frac{3}{2}}$ and $h = 1/n$, where $n = 8k$ with $k = 1, 2, \dots, 7$.

Table 5.1 presents the numerical results of the model with $\nu = 0.1$, $\mu = 1.0$, $\chi = 0.1$, $\kappa = 0.1$ and $T = 1.0$. It is evident that the errors decrease as the spatial steps diminish, with the convergence rates being optimal. To verify the robustness of the numerical method, the numerical results for various parameters in time $T = 1.0$ are presented in Tables 5.1 to 5.1. From the results, it can be observed that the errors decrease as the mesh is refined. The L^2 convergence rates for velocity, angular velocity, and temperature reach third order, while the H^1 convergence rates reach second order. The results show a good agreement between the numerical solutions and the theoretical analysis.

Table 1: Numerical results for $v=0.1, \chi=0.1, \mu=1.0, \kappa=0.1$ with various h in 2D.

$1/h$	$\ \mathbf{u}_h - \mathbf{u}\ _0$	$\ \nabla(\mathbf{u}_h - \mathbf{u})\ _0$	$\ p_h - p\ _0$	$\ \omega_h - \omega\ _0$	$\ \nabla(\omega_h - \omega)\ _0$	$\ \theta_h - \theta\ _0$	$\ \nabla(\theta_h - \theta)\ _0$
8	6.1732e-03	3.7374e-01	1.3940e-01	4.3030e-03	2.5955e-01	4.3709e-03	2.5926e-01
16	7.4497e-04	9.5095e-02	1.9781e-02	4.9888e-04	6.6827e-02	5.0054e-04	6.6812e-02
24	2.1942e-04	4.2423e-02	6.7066e-03	1.4719e-04	2.9878e-02	1.4623e-04	2.9875e-02
32	9.2460e-05	2.3892e-02	3.1722e-03	6.2173e-05	1.6842e-02	6.1486e-05	1.6841e-02
40	4.7353e-05	1.5297e-02	1.7860e-03	3.1877e-05	1.0790e-02	3.1455e-05	1.0789e-02
48	2.7405e-05	1.0625e-02	1.1213e-03	1.8477e-05	7.4970e-03	1.8203e-05	7.4968e-03
56	1.7261e-05	7.8061e-03	7.5903e-04	1.1651e-05	5.5098e-03	1.1466e-05	5.5097e-03
$1/h$	$\mathbf{u}_{\text{order}L^2}$	$\mathbf{u}_{\text{order}H^1}$	$p_{\text{order}L^2}$	$\omega_{\text{order}L^2}$	$\omega_{\text{order}H^1}$	$\theta_{\text{order}L^2}$	$\theta_{\text{order}H^1}$
16	3.0508	1.9746	2.8170	3.1086	1.9575	3.1264	1.9562
24	3.0147	1.9908	2.6676	3.0105	1.9853	3.0348	1.9849
32	3.0041	1.9958	2.6024	2.9957	1.9926	3.0116	1.9925
40	2.9987	1.9982	2.5743	2.9938	1.9954	3.0037	1.9955
48	2.9997	1.9989	2.5531	2.9912	1.9968	3.0000	1.9968
56	2.9989	2.0000	2.5313	2.9915	1.9979	2.9984	1.9978

Table 2: Numerical results for $v=0.1, \chi=0.1, \mu=1.0, \kappa=0.1$ with various h in 2D.

$1/h$	$\ \mathbf{u}_h - \mathbf{u}\ _0$	$\ \nabla(\mathbf{u}_h - \mathbf{u})\ _0$	$\ p_h - p\ _0$	$\ \omega_h - \omega\ _0$	$\ \nabla(\omega_h - \omega)\ _0$	$\ \theta_h - \theta\ _0$	$\ \nabla(\theta_h - \theta)\ _0$
8	6.3831e-04	3.7854e-01	3.3886e-02	4.2889e-03	2.5957e-01	4.3875e-03	2.5930e-01
16	7.5275e-04	9.5312e-02	5.6920e-03	5.0347e-04	6.6829e-02	5.0106e-04	6.6813e-02
24	2.2132e-04	4.2462e-02	2.2377e-03	1.4834e-04	2.9879e-02	1.4674e-04	2.9875e-02
32	9.3289e-05	2.3904e-02	1.1930e-04	6.2598e-05	1.6842e-02	6.1794e-05	1.6841e-02
40	4.7797e-05	1.5303e-02	7.4032e-04	3.2077e-05	1.0790e-02	3.1641e-05	1.0789e-02
48	2.7675e-05	1.0628e-02	5.0391e-04	1.8586e-05	7.4970e-03	1.8323e-05	7.4968e-03
56	1.7437e-05	7.8081e-03	3.6505e-04	1.1717e-05	5.5098e-03	1.1547e-05	5.5097e-03
$1/h$	$\mathbf{u}_{\text{order}L^2}$	$\mathbf{u}_{\text{order}H^1}$	$p_{\text{order}L^2}$	$\omega_{\text{order}L^2}$	$\omega_{\text{order}H^1}$	$\theta_{\text{order}L^2}$	$\theta_{\text{order}H^1}$
8	—	—	—	—	—	—	—
16	3.0840	1.9897	2.5737	3.0906	1.9576	3.1304	1.9564
24	3.0191	1.9941	2.3026	3.0139	1.9854	3.0288	1.9850
32	3.0030	1.9972	2.1865	2.9989	1.9926	3.0063	1.9925
40	2.9970	1.9987	2.1381	2.9962	1.9956	2.9997	1.9955
48	2.9971	1.9996	2.1100	2.9932	1.9970	2.9962	1.9970
56	2.9964	2.0000	2.0912	2.9930	1.9979	2.9951	1.9978

5.2 Accuracy tests in 3D

We consider the three-dimensional ($\Omega = (0,1)^3$) micropolar Rayleigh-Bénard convection system with the following exact solution:

$$\begin{cases} \mathbf{u} = (\sin(t)\sin(\pi x)\sin(\pi(y+0.5))\sin(\pi z), \sin(t)\cos(\pi x)\cos(\pi(y+0.5))\sin(\pi z), 0), \\ p = \sin(t)(2x-1)(2y-1)(2z-1), \\ \omega = (\sin(2\pi x+t), \sin(2\pi y+t), \sin(2\pi z+t)), \\ \theta = \cos(2\pi x+t)\cos(2\pi y+t)\cos(2\pi z+t). \end{cases}$$

The three-dimensional distributions of velocity, pressure, angular velocity, and temperature at time $t=1$, $h=1/32$, $\delta_t=h^2$ are plotted in Figure 1 - Figure 2. The results indicate that all

Table 3: Numerical results for $v=0.1, \chi=0.1, \mu=0.01, \kappa=0.1$ with various h in 2D.

$1/h$	$\ \mathbf{u}_h - \mathbf{u}\ _0$	$\ \nabla(\mathbf{u}_h - \mathbf{u})\ _0$	$\ p_h - p\ _0$	$\ \omega_h - \omega\ _0$	$\ \nabla(\omega_h - \omega)\ _0$	$\ \theta_h - \theta\ _0$	$\ \nabla(\theta_h - \theta)\ _0$
8	6.4267e-03	3.8252e-01	2.4320e-02	4.3786e-03	2.5964e-01	4.3623e-03	2.5929e-01
16	7.5920e-04	9.5573e-02	4.7747e-03	5.1153e-04	6.6832e-02	5.0221e-04	6.6814e-02
24	2.2340e-04	4.2528e-02	2.0077e-03	1.5035e-04	2.9879e-02	1.4764e-04	2.9876e-02
32	9.4598e-05	2.3929e-02	1.0993e-03	6.3369e-05	1.6843e-02	6.2240e-05	1.6842e-02
40	4.8512e-05	1.5313e-02	6.9091e-04	3.2450e-05	1.0790e-02	3.1935e-05	1.0790e-02
48	2.8112e-05	1.0633e-02	4.7390e-04	1.8793e-05	7.4970e-03	1.8509e-05	7.4968e-03
56	1.7723e-05	7.8108e-03	3.4549e-04	1.1844e-05	5.5098e-03	1.1671e-05	5.5097e-03
$1/h$	$\mathbf{u}_{\text{order}L^2}$	$\mathbf{u}_{\text{order}H^1}$	$p_{\text{order}L^2}$	$\omega_{\text{order}L^2}$	$\omega_{\text{order}H^1}$	$\theta_{\text{order}L^2}$	$\theta_{\text{order}H^1}$
8	—	—	—	—	—	—	—
16	3.0815	2.0009	2.3487	3.0976	1.9579	3.1187	1.9563
24	3.0170	1.9970	2.1367	3.0198	1.9854	3.0194	1.9850
32	2.9871	1.9990	2.0937	3.0033	1.9925	3.0025	1.9924
40	2.9928	2.0005	2.0813	2.9993	1.9956	2.9904	1.9954
48	2.9926	2.0005	2.0678	2.9959	1.9971	2.9917	1.9973
56	2.9927	2.0010	2.0502	2.9949	1.9979	2.9916	1.9978

Table 4: Numerical results for $v=0.1, \chi=0.1, \mu=0.001, \kappa=0.1$ with various h in 2D.

$1/h$	$\ \mathbf{u}_h - \mathbf{u}\ _0$	$\ \nabla(\mathbf{u}_h - \mathbf{u})\ _0$	$\ p_h - p\ _0$	$\ \omega_h - \omega\ _0$	$\ \nabla(\omega_h - \omega)\ _0$	$\ \theta_h - \theta\ _0$	$\ \nabla(\theta_h - \theta)\ _0$
8	6.4307e-03	3.8350e-01	2.3522e-02	4.4017e-03	2.5965e-01	4.3582e-03	2.5929e-01
16	7.6082e-04	9.5647e-02	4.7114e-03	5.1356e-04	6.6833e-02	5.0267e-04	6.6815e-02
24	2.2467e-04	4.2546e-02	1.9901e-03	1.5086e-04	2.9879e-02	1.4790e-04	2.9876e-02
32	9.4920e-05	2.3935e-02	1.0910e-03	6.3568e-05	1.6843e-02	6.2434e-05	1.6842e-02
40	4.8688e-05	1.5316e-02	6.8632e-04	3.2547e-05	1.0790e-02	3.2011e-05	1.0790e-02
48	2.8218e-05	1.0634e-02	4.7115e-04	1.8847e-05	7.4970e-03	1.8556e-05	7.4968e-03
56	1.7793e-05	7.8114e-03	3.4381e-04	1.1877e-05	5.5098e-03	1.1702e-05	5.5097e-03
$1/h$	$\mathbf{u}_{\text{order}L^2}$	$\mathbf{u}_{\text{order}H^1}$	$p_{\text{order}L^2}$	$\omega_{\text{order}L^2}$	$\omega_{\text{order}H^1}$	$\theta_{\text{order}L^2}$	$\theta_{\text{order}H^1}$
8	—	—	—	—	—	—	—
16	3.0793	2.0034	2.3198	3.0995	1.9579	3.1160	1.9563
24	3.0083	1.9979	2.1255	3.0213	1.9855	3.0173	1.9851
32	2.9950	1.9996	2.0894	3.0042	1.9925	2.9978	1.9924
40	2.9918	2.0007	2.0772	3.0000	1.9956	2.9937	1.9954
48	2.9918	2.0011	2.0632	2.9965	1.9971	2.9908	1.9973
56	2.9916	2.0011	2.0440	2.9954	1.9979	2.9908	1.9978

physical quantities are uniformly distributed. To verify the accuracy of the numerical scheme, we compute the errors and convergence rates. As shown in Table 5.2, the spatial mesh sizes are taken as $h = 1/n$, where $n = 4k$ with $k = 2, 3, \dots, 8$, and the time step is set to $\delta_t = h^2$. From the results, it can be observed that the errors decrease as the mesh is refined. The L^2 convergence rates for velocity, angular velocity, and temperature attain third order, while the corresponding H^1 convergence rates attain second order, all of which are optimal and consistent with the theoretical predictions.

Table 5: Numerical results for $v=1.0, \chi=1.0, \mu=1.0, \kappa=1.0$ with various h in 3D.

$1/h$	$\ \mathbf{u}_h - \mathbf{u}\ _0$	$\ \nabla(\mathbf{u}_h - \mathbf{u})\ _0$	$\ p_h - p\ _0$	$\ \omega_h - \omega\ _0$	$\ \nabla(\omega_h - \omega)\ _0$	$\ \theta_h - \theta\ _0$	$\ \nabla(\theta_h - \theta)\ _0$
8	7.6130e-04	5.3669e-02	1.5355e-02	3.3160e-03	1.7524e-01	6.2245e-03	3.3628e-01
12	2.2484e-04	2.4161e-02	3.8462e-03	9.8079e-04	7.8294e-02	1.7056e-03	1.5665e-01
16	9.4811e-05	1.3656e-02	1.5023e-03	4.1404e-04	4.4122e-02	6.8933e-04	8.9855e-02
20	4.8506e-05	8.7564e-03	7.6056e-04	2.1255e-04	2.8262e-02	3.4461e-04	5.8076e-02
24	2.8023e-05	6.0827e-03	4.5769e-04	1.2370e-04	1.9636e-02	1.9662e-04	4.0557e-02
28	1.7536e-05	4.4672e-03	3.0906e-04	7.8866e-05	1.4430e-02	1.2270e-04	2.9901e-02
32	1.1892e-05	3.4234e-03	2.2695e-04	5.4536e-05	1.1051e-02	8.1747e-05	2.2946e-02
$1/h$	$\mathbf{u}_{\text{order}L^2}$	$\mathbf{u}_{\text{order}H^1}$	$p_{\text{order}L^2}$	$\omega_{\text{order}L^2}$	$\omega_{\text{order}H^1}$	$\theta_{\text{order}L^2}$	$\theta_{\text{order}H^1}$
8	—	—	—	—	—	—	—
12	3.0080	1.9683	3.4142	3.0043	1.9871	3.1930	1.8842
16	3.0016	1.9833	3.2677	2.9977	1.9936	3.1491	1.9320
20	3.0035	1.9915	3.0506	2.9882	1.9962	3.1070	1.9559
24	3.0093	1.9983	2.7855	2.9688	1.9974	3.0779	1.9693
28	3.0410	2.0025	2.5473	2.9201	1.9981	3.0586	1.9774
32	2.9087	1.9928	2.3125	2.7626	1.9984	3.0415	1.9828

5.3 Stirring of a passive scalar

In fluid dynamics, a passive scalar, such as temperature, concentration, or dye, is transported by the flow without affecting it. This numerical experiment confirms the stability of the second-order pressure projection scheme and its potential for engineering applications. In laminar flows, weak diffusion limits mixing and slows reactant dispersion. Active ferromagnetic nanoparticles can overcome this limitation by being manipulated with external magnetic fields to stir the fluid and enhance passive scalar transport. The dynamics of such systems can be modeled using the micropolar Navier-Stokes equations[44, 45, 46]. In this work, we adopt the micropolar Rayleigh-Bénard convection system to describe and analyze this process.

We consider system (2.1) in the domain $\Omega = (-1, 1)^2$ and set $v=2.0, \chi=0.1, \kappa=1.0$ and $\mu=0.1$. The micropolar Rayleigh-Bénard convection system is further supplemented with a convective equation given by

$$\phi_t + (\mathbf{u} \cdot \nabla)\phi = 0, \phi_{t=0} = 0.5(1 - \tanh(y/\delta)), \quad \delta = 0.5h.$$

There is no diffusion term in this equation, so any observed mixing is solely induced by the flow pattern. To avoid nonphysical undershoot or overshoot caused by numerical dispersion, a simple limiter is applied at each time step: $\phi(x) \leftarrow \min(1, \max(0, \phi(x)))$. This limiter ensures that the scalar field ϕ remains within the physically admissible bounds throughout the simulation. The velocity, angular velocity field and pressure field at time $t=50$ are displayed in Figure 3. Due to the applied torque $f_w = 25(x-1)$, the linear velocity field \mathbf{u} exhibits a rotational pattern, as shown in Figure 3(a). Figure 4 illustrates the temporal evolution of the passive scalar ϕ under the applied laminar flow. Initially, ϕ is initialized as a smooth profile (Figure 4(a)), which is gradually deformed and stretched by the flow field over time. As the simulation progresses, the scalar exhibits complex spiral structures due to continuous advection, indicating enhanced mixing (Figure 4(b)-Figure 4(n)). By $t=50$, the scalar distribution demonstrates a highly folded pattern,

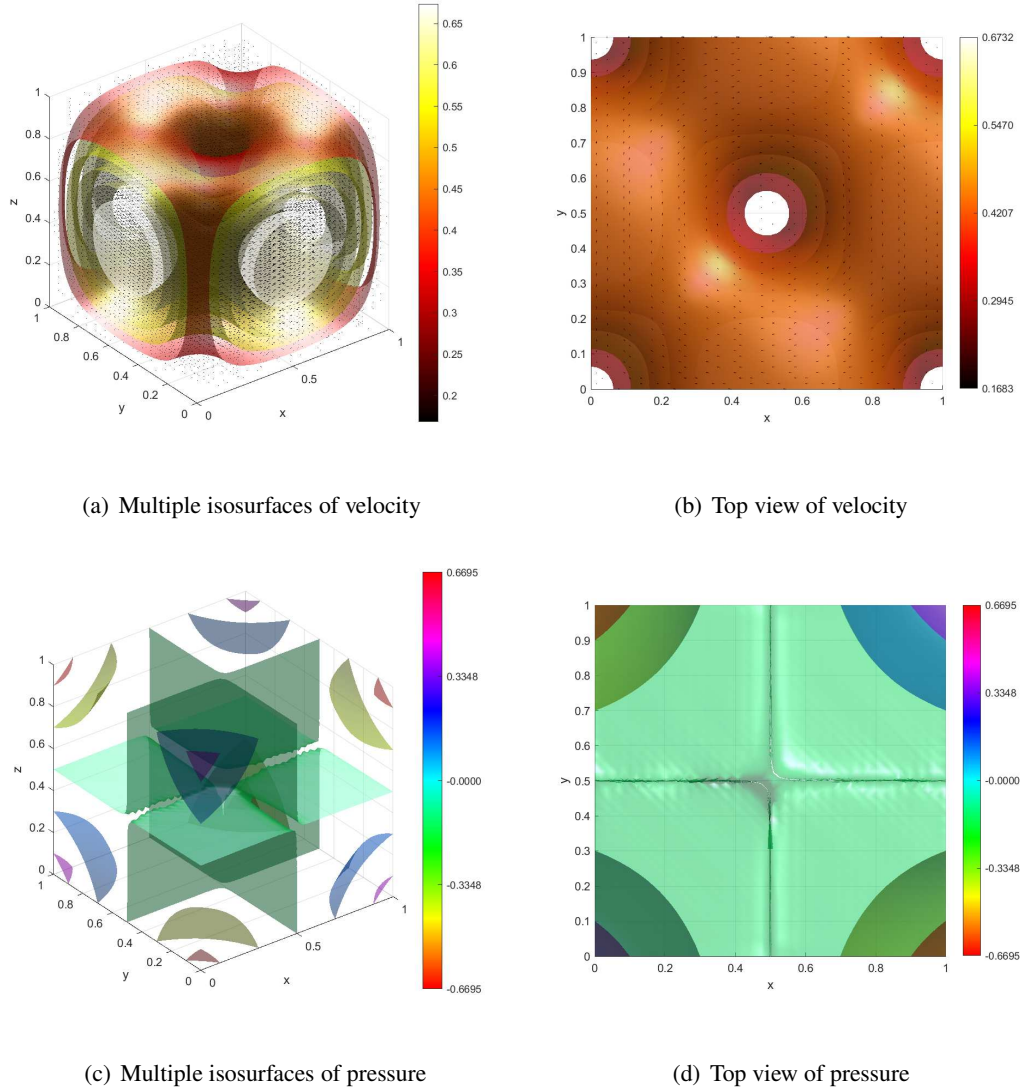


Figure 1: Numerical distributions of the velocity and pressure.

suggesting that the flow efficiently enhances the dispersion of the passive scalar. This sequence not only confirms the stability of the numerical scheme but also visualizes the mixing process induced by the underlying velocity field.

5.4 Driven cavity flows in 2D

In this subsection, the stability of the second-order pressure projection scheme is validated through a lid-driven cavity flow in 2D with a simple heating distribution. The computational domain is

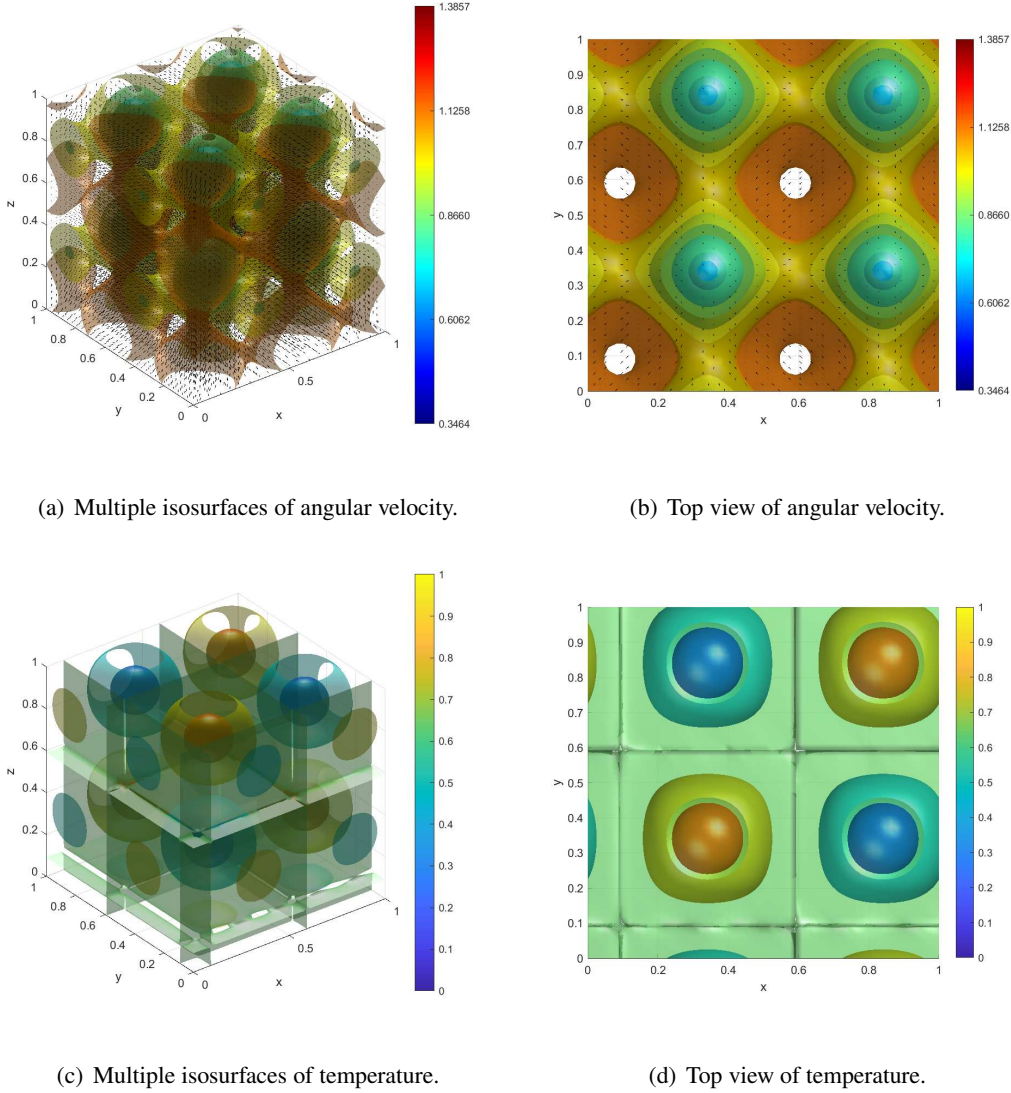


Figure 2: Numerical distributions of the angular velocity and temperature.

defined as the unit square $\Omega = (0,1)^2$. The initial conditions are given by $\omega_0 = 0, \theta_0 = 0$ and $\mathbf{u}_0 = (0,0)$. The boundary conditions are given as follows: the top lid applies a horizontal velocity $\mathbf{u}_1 = (1,0)$, while the other boundaries adopt a no-slip boundary condition $\mathbf{u} = (0,0)$. The angular velocity satisfies $\omega = 0$; for the temperature, $\theta = 1.0$ is prescribed on the right boundary, $\theta = 0$ on the left boundary, and $\frac{\partial \theta}{\partial n} = 0$ on the upper and lower boundaries. The spatial step is chosen as $h = 1/80$ and the time step is $\delta_t = 10^{-3}$. The finite element spaces is chosen as $P2-P1$. In order to verify the influence of the top and thermal drives in the system, we set the following

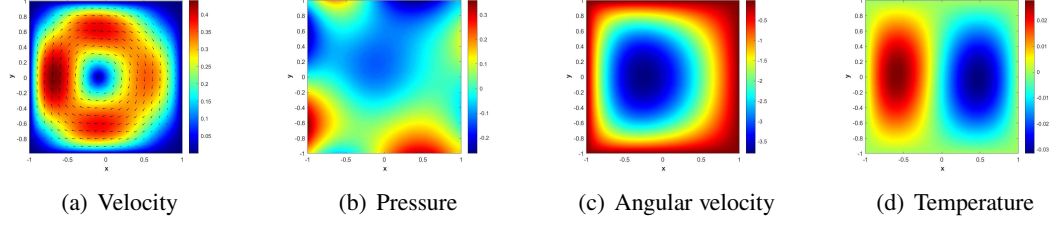


Figure 3: Distribution map of numerical solutions for velocity \mathbf{u} , angular velocity w , pressure p and temperature θ at $t=50$.

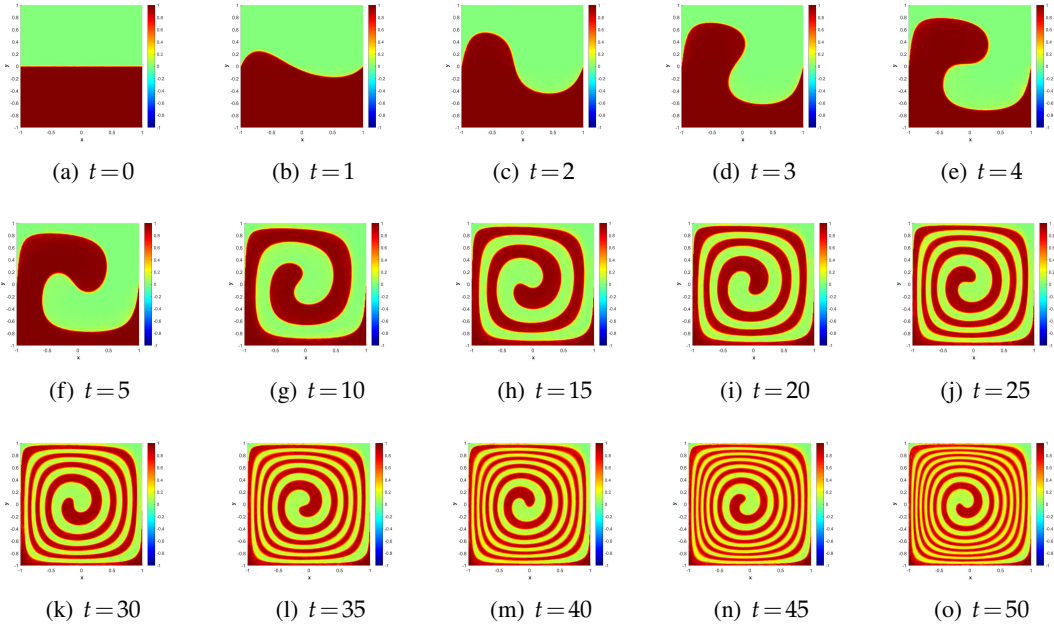


Figure 4: Mixing evolution of a convected passive scalar ϕ over time. Each subfigure shows the scalar field at a specific time t . For better visual comparison, the color axis is fixed to $[-1, 1]$, although the actual scalar field ϕ is constrained in $[0, 1]$

parameters. Since the buoyancy drive term $e\theta$ in the system, we use a normalization process. Using the system parameters, the Rayleigh number has the following expression $Ra = \frac{1}{(\chi + \mu)\kappa}$. In Figure 5–Figure 8, the physical parameters are set as $v=1.0$, $\kappa=0.01$, and $\chi=\mu=0.1, 0.01, 0.001$, and 0.0001 respectively. As shown in Figure 5, when $Ra=50$ and $Ra=500$, the thermal driving force is weak, and the flow is primarily dominated by the motion of the top lid. In contrast, for $Ra=5000$ and $Ra=50000$, the thermal effect competes with the lid-driven motion, leading to the emergence of a mixed flow pattern. This phenomenon is also clearly observed in the contour plots of pressure, angular velocity, and temperature. These results further confirm the effectiveness of the proposed second-order pressure projection scheme, as the velocity, angular velocity, pressure,

and temperature fields all converge toward a steady state.

To further investigate the influence of microspin on the fluid behavior, we designed a series of numerical experiments with different sets of physical parameters: $\kappa = \chi = \mu = 0.1$, and $\nu = 1.0, 0.01, 0.001$, and 0.0001 , respectively. From Figure 9, it can be observed that for $\nu = 1.0$, the microspin effect strongly suppresses local variations in angular velocity, leading to a smooth angular velocity field with a very small amplitude, on the order of 10^{-3} . As ν decreases, the response of the angular velocity becomes more pronounced: local peaks and shear-layer structures emerge, particularly near the wall, and the maximum amplitude of angular velocity increases with a sharper spatial distribution. This trend indicates that weaker microspin diffusion enhances the degrees of freedom of the angular motion and intensifies microrotation activity within the system, which is consistent with the fundamental predictions of micropolar fluid theory.

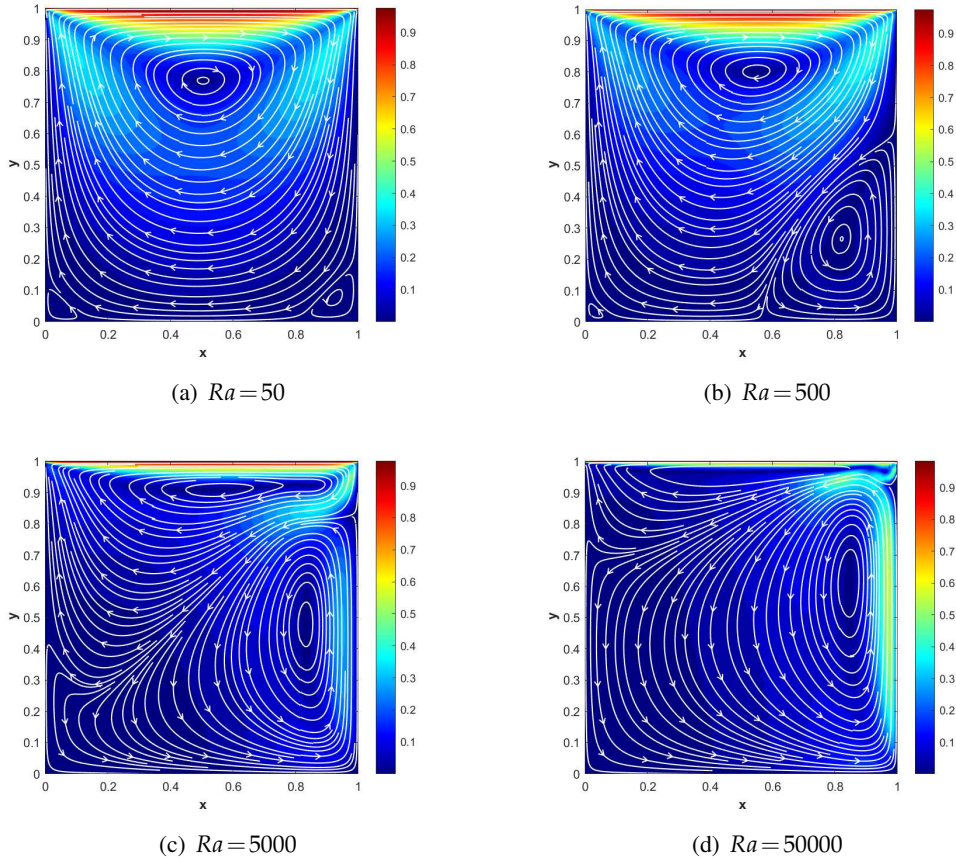


Figure 5: Visualization of the numerical solution distribution for streamlines.

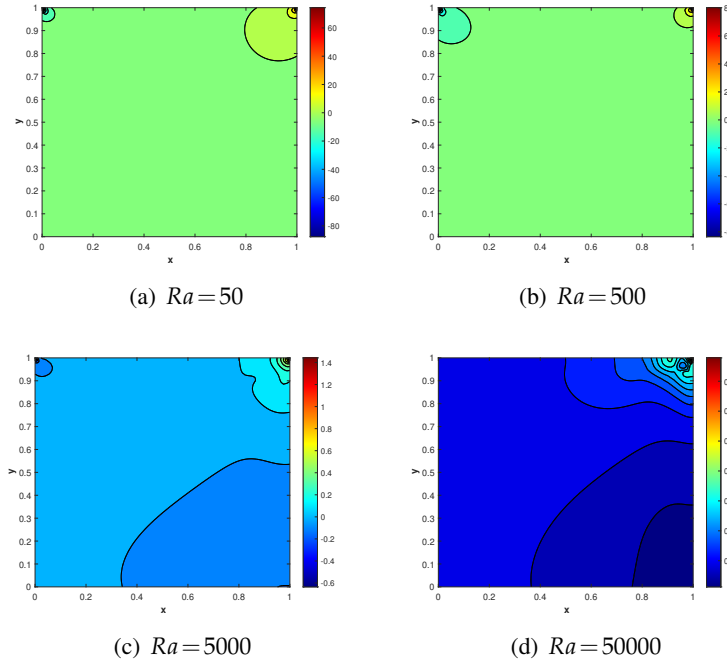


Figure 6: Visualization of the numerical solution distribution for pressure.

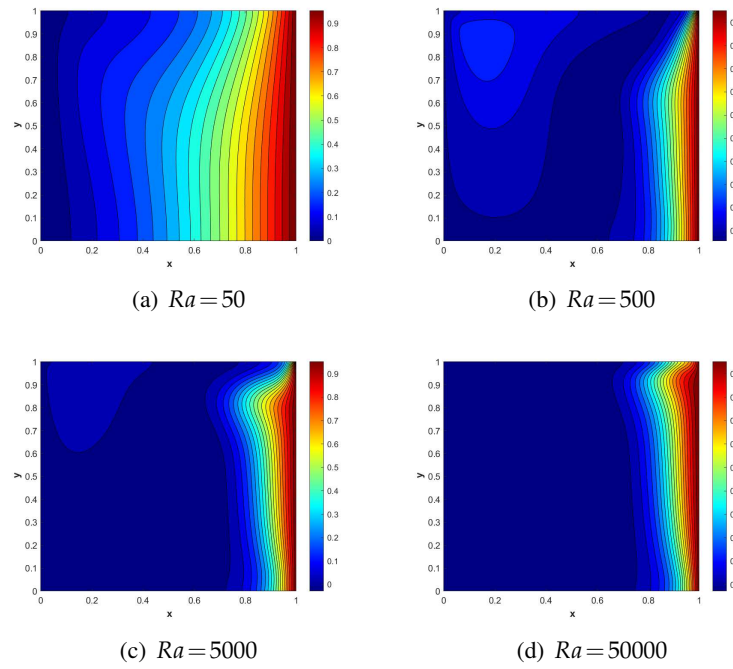


Figure 7: Visualization of the numerical solution distribution for temperature.

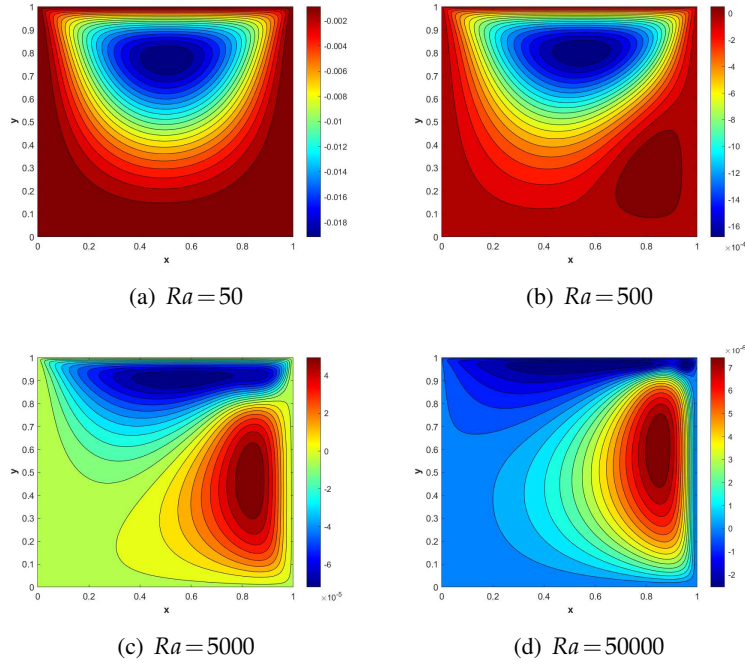


Figure 8: Visualization of the numerical solution distribution for angular velocity.

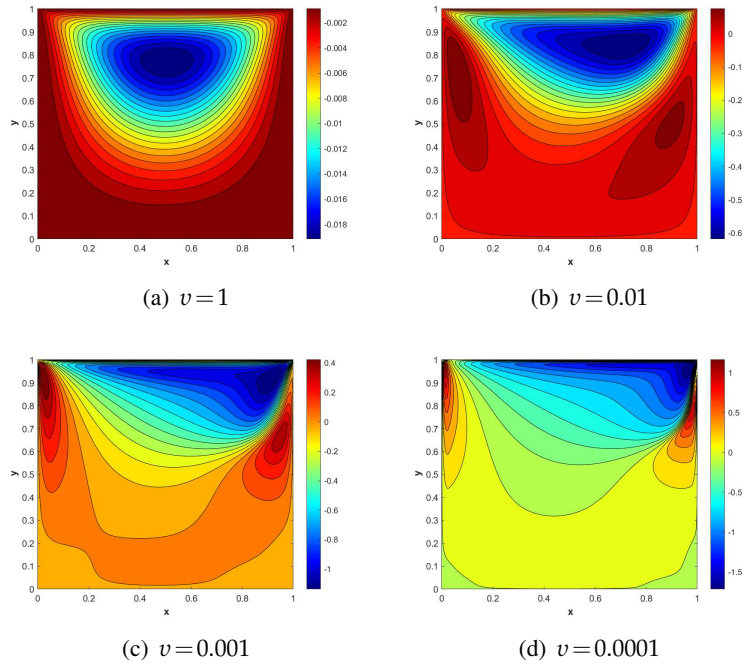


Figure 9: Visualization of the numerical solution distribution for angular velocity.

6 Conclusions

The micropolar Rayleigh-Bénard convection system is a strongly coupled system, resulting in expensive computations for traditional coupled algorithms. With spatial discretization of the finite element method, a numerical scheme possessing the favorable properties of linearity, full decoupling, and second-order time accuracy is constructed. Based on a second-order projection technique for the hydrodynamic component, the scheme exhibits significant computing efficiency with only a few independent linear elliptic subproblems with constant coefficients at each time step. This work not only conducts a rigorous stability analysis, but also employs the inverse Stokes operator and negative-norm estimates to effectively address the convergence-order reduction caused by the pressure term, thereby achieving optimal error estimates. The effectiveness and robustness of the scheme are presented with numerical experiments, including precision tests, temperature-driven cavity flow simulations, and the stirring of a passive scalar experiment. In future research, the model will be extended to the magneto-micropolar fluids, where the Maxwell equations are coupled to describe the influence of external magnetic and electric fields on micro-particle rotation. This coupling is expected to enable active control of microrotation dynamics through electromagnetic fields.

Acknowledgments

Ming Cui's work was supported by National Natural Science Foundation of China No. 12371368. Xiaoyu Dong's work was supported by the Postdoctoral Fellowship Program of CPSF under Grant No. GZC20251999 and the Beijing Postdoctoral Research Foundation under Grant No. 2025-ZZ-34.

References

- [1] A.C. Eringen. Theory of micropolar fluids. *Journal of Mathematics and Mechanics*, 16: 1–18, 1966.
- [2] H. Bahouri, J.Y. Chemin, and R. Danchin. *Fourier analysis and nonlinear partial differential equations*. Grundlehren der Mathematischen Wissenschaften. Springer, Heidelberg, 2011.
- [3] J. Beale, T. Kato, and A. Majda. Remarks on the breakdown of smooth solutions for the 3-d Euler equations. *Communications in Mathematical Physics*, 94:61–66, 1984.
- [4] A. Popel, S. Regirer, and P. Usick. A continuum model of blood flow. *Biorheology*, 11: 427–437, 1974.
- [5] C. Foias, O. Manley, and R. Temam. Attractors for the Bénard problem: existence and physical bounds on their fractal dimension. *Nonlinear Analysis: Theory, Methods & Applications*, 11 (8):939–967, 1987.

- [6] P. Kalita, J. Langa, and G. Lukaszewicz. Micropolar meets Newtonian. the Rayleigh-Bénard problem. *Physica D: Nonlinear Phenomena*, 392:57–80, 2019.
- [7] A. Tarasinska. Global attractor for heat convection problem in a micropolar fluid. *Mathematical Methods in the Applied Sciences*, 29:1215–1236, 2006.
- [8] F. Xu and M. Chi. Global regularity for the 2d micropolar Rayleigh-Bénard convection system with the zero diffusivity. *Applied Mathematics Letters*, 108:106508, 2020.
- [9] Ajay Choudhary, Kirti Sahu, and Suman Chandra. Rayleigh-Bénard instability in nanofluids: a comprehensive review. *Microfluidics and Nanofluidics*, 24(6):1–21, 2020.
- [10] M. Turkyilmazoglu. Laminar flow and heat transfer of a micropolar fluid over a stretching sheet. *International Journal of Heat and Mass Transfer*, 72:686–694, 2014.
- [11] P. Rana and R. Bhargava. Flow and heat transfer of a nanofluid over a nonlinearly stretching sheet: a numerical study. *Communications in Nonlinear Science and Numerical Simulation*, 17(1):212–226, 2012.
- [12] J. H. He. Homotopy perturbation technique. *Computer Methods in Applied Mechanics and Engineering*, 178:257–262, 1999.
- [13] Orhan Aydn and Ioan Popb. Natural convection in a differentially heated enclosure filled with a micropolar fluid. *International Journal of Thermal Sciences*, 46:963–969, 2007.
- [14] A. J. Chorin. Numerical solution of the Navier-Stokes equations. *Mathematics of Computation*, 22:745–762, 1968.
- [15] R. Temam. Sur l’approximation de la solution des equations de navier-stokes par la methode des pas fractionnaires (ii). *Archive for Rational Mechanics and Analysis*, 33:377–385, 1969.
- [16] R. Rannacher. *On Chorin’s projection method for the incompressible Navier-Stokes equations*, volume 1530 of *Lecture Notes in Mathematics*. Springer, Berlin, 1992.
- [17] H. C. Ku, R. S. Hirsh, and T. D. Taylor. A pseudospectral method for solution of the three-dimensional incompressible Navier-Stokes equations. *Journal of Computational Physics*, 70:439–462, 1987.
- [18] J. B. Bell, P. Colella, and H. M. Glaz. A second order projection method for the incompressible Navier-Stokes equations. *Journal of Computational Physics*, 85:257–283, 1989.
- [19] J. L. Guermond and Jean-Luc. Some Implementations of Projection Methods for Navier-Stokes Equations. *ESAIM: Mathematical Modelling and Numerical Analysis*, 30(5):637–667, 1996.
- [20] J. L. Guermond and L. Quartapelle. On the approximation of the Navier-Stokes equations by finite element projection. *Numerische Mathematik*, 80:207–238, 1998.

- [21] J. L. Guermond and Jean-Luc. Un Résultat de Convergence D'ordre Deux En Temps Pour L'approximation Des Équations de Navier-Stokes Par Une Technique de Projection-incrémentale. *ESAIM: Mathematical Modelling and Numerical Analysis*, 33(1):169–189, 1999.
- [22] G. Zhang, X. He, and X. Yang. Decoupled, linear, and unconditionally energy stable fully discrete finite element numerical scheme for a two-phase ferrohydrodynamics model. *SIAM Journal on Scientific Computing*, 43:167–193, 2021.
- [23] G. Zhang, X. He, and X. Yang. Reformulated weak formulation and efficient fully discrete finite element method for a two-phase ferrohydrodynamics shliomis model. *SIAM Journal on Scientific Computing*, 45:B253–B282, 2023.
- [24] G. Zhang, X. He, and X. Yang. A unified framework of the sav-zec method for a mass-conserved allen-cahn type two-phase ferrofluid flow model. *SIAM Journal on Scientific Computing*, 46:B77–B106, 2024.
- [25] J. Pyo. Optimal error estimate for semi-discrete Gauge-Uzawa method for the Navier-Stokes equations. *Bulletin of the Korean Mathematical Society*, 46:627–644, 2009.
- [26] J. Pyo. Error estimate for the second order semi-discrete stabilized gauge-uzawa method for the navier-stokes equations. *International Journal of Numerical Analysis & Modeling*, 10: 24–41, 2013.
- [27] Z. Si, M. Wang, and Y. Wang. A projection method for the non-stationary incompressible mhd coupled with the heat equations. *Applied Mathematics and Computation*, 428:127217, 2022.
- [28] J. Guermond and J. Shen. Velocity-correction projection methods for incompressible flows. *SIAM Journal on Numerical Analysis*, 41(1):112–134, 2003.
- [29] Z. Si, J. Lu, and Y. Wang. Unconditional stability and error estimates of the modified characteristics fems for the time-dependent thermally coupled incompressible mhd equations. *Computers and Fluids*, 240:105427, 2022.
- [30] F. Xu, L. Qiao, and M. Zhang. On the well-posedness for the 2d micropolar rayleigh-bénard convection problem. *Zeitschrift für angewandte Mathematik und Physik (ZAMP)*, 72(17), 2021.
- [31] B. Yuan and C. Li. Global regularity for the 2d Micropolar Rayleigh-Bénard Convection System with Velocity Zero Dissipation and Temperature Critical Diffusion. *Mathematical Methods in the Applied Sciences*, 47(9):7502–7517, 2024.
- [32] G. Galdi. *An Introduction to the Mathematical Theory of the Navier-Stokes Equations: Steady-State Problems*. Springer, New York, 2011.

- [33] F. Brezzi and M. Fortin. *Mixed and hybrid finite element methods*. Springer, New York, 1991.
- [34] S. Brenner and L. Scott. *The mathematical theory of finite element methods*. Springer, New York, 1994.
- [35] V. Girault and P. Raviart. *Finite element methods for the Navier-Stokes equations*. Springer, New York, 1986.
- [36] Y. He and J. Li. Convergence of three iterative methods based on the finite element discretization for the stationary navier-stokes equations. *Computer Methods in Applied Mechanics and Engineering*, 198:1351–1359, 2009.
- [37] Y. He. Unconditional convergence of the euler semi-implicit scheme for the three-dimensional incompressible mhd equations. *IMA Journal of Numerical Analysis*, 35:767–801, 2015.
- [38] R. Temam. *Navier-Stokes Equations: Theory and Numerical Analysis*. North-Holland, Amsterdam, 1984. MR 58:29439.
- [39] Y. Lei, Y. Yang, and Z. Si. Error estimate of a fully discrete defect correction finite element method for unsteady incompressible magnetohydrodynamics equations. *Applicable Analysis*, 97:2355–2376, 2018.
- [40] Lin Che and Zey. Convergence Analysis of a bdf Finite Element Method for the Resistive Magnetohydrodynamic Equations. *Advances in Applied Mathematics and Mechanics*, 17(2): 633–662, 2025.
- [41] J. Shen. Remarks on the pressure error estimates for the projection methods. *Numerische Mathematik*, 67(4):513–520, 1994.
- [42] J. Heywood and R. Rannacher. Finite-element approximation of the nonstationary Navier-Stokes problem. i. regularity of solutions and second-order error estimates for spatial discretization. *SIAM Journal on Numerical Analysis*, 19(2):275–311, 1982.
- [43] F. Hecht. New development in Freefem++. *Journal of Numerical Mathematics*, 20:251–265, 2012.
- [44] K. R. Rajagopal. Flow of a Viscoelastic Micropolar Fluid Between Two Porous Discs. *Acta Mechanica*, 44(3-4):219–229, 1982.
- [45] K. Khanafer, K. Vafai, and M. Lightstone. Buoyancy-driven heat transfer enhancement in a two-dimensional enclosure utilizing nanofluids. *International Journal of Heat and Mass Transfer*, 46(19):3639–3653, 2003.
- [46] G. Zhang, Q. Huang, X. He, and X. Yang. Efficient Fully Discrete and Decoupled Scheme with Unconditional Energy Stability and Second-Order Accuracy for Micropolar Navier-Stokes Equations. *Computer Methods in Applied Mechanics and Engineering*, 436:117692, 2025.